

RESEARCH ARTICLE

10.1029/2020JD033074

Anthropogenic Impacts on Atmospheric Carbonyl Sulfide Since the 19th Century Inferred From Polar Firn Air and Ice Core Measurements

Key Points:

- We conducted a simultaneous multisite inversion of firn air COS data from Greenland and Antarctic ice sheets for the first time
- Analysis provides hemispheric records of atmospheric COS that display large increases through the first 70–80 years of the 20th century
- Model results suggest anthropogenic emissions are the primary driver of decadal changes in atmospheric COS levels during the study period

Supporting Information:

- Supporting Information S1
- Data Set S1
- Data Set S2

Correspondence to:

M. Aydin,
maydin@uci.edu

Citation:

Aydin, M., Britten, G. L., Montzka, S. A., Buizert, C., Primeau, F., Petrenko, V., et al. (2020). Anthropogenic impacts on atmospheric carbonyl sulfide since the 19th century inferred from polar firn air and ice core measurements. *Journal of Geophysical Research: Atmospheres*, 125, e2020JD033074. <https://doi.org/10.1029/2020JD033074>

Received 11 MAY 2020

Accepted 29 JUL 2020

Accepted article online 3 AUG 2020

M. Aydin¹ , G. L. Britten^{1,2} , S. A. Montzka³ , C. Buizert⁴ , F. Primeau¹ , V. Petrenko⁵ , M. B. Battle⁶ , M. R. Nicewonger^{1,3} , J. Patterson¹ , B. Hmiel⁵ , and E. S. Saltzman¹ 

¹Department of Earth System Science, University of California, Irvine, Irvine, CA, USA, ²Department of Earth, Atmospheric, and Planetary Sciences, Massachusetts Institute of Technology, Cambridge, MA, USA, ³Global Monitoring Laboratory, National Oceanic and Atmospheric Administration, Boulder, CO, USA, ⁴College of Earth, Ocean, and Atmospheric Sciences, Oregon State University, Corvallis, OR, USA, ⁵Department of Earth and Environmental Sciences, University of Rochester, Rochester, NY, USA, ⁶Department of Physics and Astronomy, Bowdoin College, Brunswick, ME, USA

Abstract Carbonyl sulfide (COS) was measured in firn air collected during seven different field campaigns carried out at four different sites in Greenland and Antarctica between 2001 and 2015. A Bayesian probabilistic statistical model is used to conduct multisite inversions and to reconstruct separate atmospheric histories for Greenland and Antarctica. The firn air inversions cover most of the 20th century over Greenland and extend back to the 19th century over Antarctica. The derived atmospheric histories are consistent with independent surface air time series data from the corresponding sites and the Antarctic ice core COS records during periods of overlap. Atmospheric COS levels began to increase over preindustrial levels starting in the 19th century, and the increase continued for much of the 20th century. Atmospheric COS peaked at higher than present-day levels around 1975 CE over Greenland and around 1987 CE over Antarctica. An atmosphere/surface ocean box model is used to investigate the possible causes of observed variability. The results suggest that changes in the magnitude and location of anthropogenic sources have had a strong influence on the observed atmospheric COS variability.

Plain Language Summary Carbonyl sulfide (COS) is the most abundant sulfur containing trace gas in the atmosphere. We measured COS in firn air collected during several different field campaigns carried out at Greenland and Antarctic ice sheets. Firn air is the unincorporated old air found between the surface snow and the underlying ice that can be used to determine past changes in atmospheric composition. Firn air COS measurements were used to determine atmospheric COS variability since the 19th century. In our analysis, we also make use of measurements of COS in ice core air that provide information atmospheric COS levels during the 17th and 18th centuries. The results demonstrate that atmospheric COS increased from a stable preindustrial background level starting in the 19th century and peaked around 1975 CE over Greenland and around 1987 CE over Antarctica. The increase is on the order of 60% and is primarily driven by emissions linked various human activities.

1. Introduction

Carbonyl sulfide (COS) is the most abundant sulfur gas in the troposphere. The global average mixing ratio of COS was 480–490 parts per trillion (ppt) during 2000–2006 CE (Montzka et al., 2007). The atmospheric lifetime of COS is estimated to be about 2 years (Berry et al., 2013). COS is a precursor of background sulfate aerosol in the stratosphere (Crutzen, 1976), although there is some uncertainty regarding the importance of COS relative to volcanic and anthropogenic SO₂ (e.g., Brühl et al., 2012; Chin & Davis, 1995; Myhre et al., 2004; Notholt et al., 2003; Solomon et al., 2011; Vernier et al., 2011). A recent modeling study suggests COS alone accounts for more than half of stratospheric aerosol during volcanically quiet periods (Sheng et al., 2015), but the net climate impact of COS may be small because the cooling effect from COS-derived stratospheric aerosol is offset by radiative greenhouse warming from tropospheric COS (Brühl et al., 2012).

Atmospheric COS is also of scientific interest because the primary removal mechanism from the atmosphere is uptake by terrestrial vegetation (Goldan et al., 1988; Kesselmeier & Merk, 1993; Kjellström, 1998;

Sandoval-Soto et al., 2005; Xu et al., 2002). During photosynthesis, terrestrial plants take up COS along with CO₂ because the carbonic anhydrase enzyme that hydrolyzes CO₂ also efficiently hydrolyzes COS (Asaf et al., 2013; Protoschill-Krebs et al., 1996; Protoschill-Krebs & Kesselmeier, 1992). Unlike CO₂, COS is generally not produced during plant respiration, although some exceptions have been identified (Gimeno et al., 2017; Wohlfahrt, 2017). Photosynthetic uptake dominates the seasonal variability of atmospheric COS in the Northern Hemisphere (NH), resulting in a late boreal summer minimum at most NH sites (Montzka et al., 2007). It is commonly assumed that the removal of atmospheric COS covaries with the globally integrated gross primary productivity (GPP) of land plants (Montzka et al., 2007; Whelan et al., 2018).

Direct and indirect emissions from the world ocean constitute the largest source of atmospheric COS (Chin & Davis, 1993; Kettle et al., 2001, 2002; Ulshöfer & Andreae, 1998; Watts, 2000). In the surface ocean, sulfur-containing organic compounds are photochemically broken down to produce COS and CS₂, which are emitted to the atmosphere via air/sea gas transfer. In the atmosphere, CS₂ is photochemically oxidized with a lifetime of several days and a COS yield of about 50%. Dimethylsulfide (DMS) is another indirect oceanic COS source. It is biologically produced in the surface ocean in large amounts and is the dominant flux of reduced sulfur to the atmosphere (Lana et al., 2011). Laboratory experiments have identified a small yield of COS (~1%) from gas phase photooxidation of DMS (Arsene et al., 2001). Because of the very large DMS flux, this source is a significant term in the COS budget.

Anthropogenic sulfur gas emissions (CS₂ and COS) from the synthetic fiber, aluminum, and coal industries are thought to be the second most important COS source in the present-day atmosphere (Campbell et al., 2015; Sturges et al., 2001). Biomass burning is another significant atmospheric COS source, with possible minor emissions from anoxic soils, wetlands, and volcanoes (Berry et al., 2013; Kettle et al., 2002; Suntharalingam et al., 2008; Watts, 2000). The ocean sources dominate the seasonal variability of COS in the Southern Hemisphere (SH), resulting in an austral summer maximum in the high-latitude SH (Montzka et al., 2007).

The first reported measurements of COS in firn air are from one Arctic (Devon Island, Canada) and two Antarctic (Dronning Maud Land and Dome Concordia) sites and imply a decline in anthropogenic COS emissions during the late 20th century (Sturges et al., 2001). A firn air study from the South Pole revealed a sharp COS increase of up to 200 ppt during the early to mid-20th century, followed by a relatively modest decline during the 1990s (Montzka et al., 2004). These trends have primarily been attributed to changes in anthropogenic emissions. Campbell et al. (2017) reanalyzed the same trends using updated estimates of sources and sinks and inferred a large growth in terrestrial GPP during the 20th century attributed to the fertilizing effect of increasing atmospheric CO₂ concentrations.

In this study, we analyze new COS measurements from six firn air sampling campaigns along with the previously published measurements from the South Pole 2001 campaign. Three of the new data sets are from Greenland: two from campaigns at Summit conducted in May 2006 and June 2013 and one from a Renland campaign carried out in 2015. The other three are from Antarctica conducted at the South Pole in December 2008/January 2009 and in December 2015, and at Mega Dunes in January 2004. We use established firn air models (Aydin et al., 2011; Buizert et al., 2012) to characterize the age of COS in firn air at each of these sites and perform Bayesian inversions to recover one SH and one NH atmospheric history consistent with all firn air COS measurements from Antarctica and Greenland. The inversions are conducted with the Stan probabilistic programming language, which uses a fast Hamiltonian Markov Chain Monte Carlo (MCMC) sampling algorithm (Carpenter et al., 2017). Antarctic ice core measurements are incorporated in the Antarctic inversions. A coupled atmosphere/surface ocean box model is used to explore the possible causes of the long-term trends in the atmospheric COS records. Implications for the atmospheric COS budget are discussed.

2. Firn Air Sampling and Measurements

Greenland firn was sampled during two different campaigns to Summit in May 2006 (SUM06) and in June 2013 (SUM13), and another one to Renland in May 2015 (REN15). Antarctic firn was sampled during three different campaigns to South Pole in December–January 2001–2002 (SPO01), in December–January 2008–2009 (SPO08), and in December 2015 (SPO15), and another campaign to Megadunes in January 2004

(MD03). The firn air trace gas sampling techniques used in these studies have been described previously (Aydin et al., 2011; Hmiel et al., 2020; Montzka et al., 2004; Mühle et al., 2019). The firn holes are dry-drilled using either a 3" or a 4" electro-mechanical drill. Once the desired sampling depth is reached, a 4 m-long bladder (natural rubber) is lowered into the hole and inflated in place to seal the bottom ~20 cm of the hole from the overlying atmosphere. There are three lines running from the surface to, or through, the bladder. One connects directly to the bladder and is used for inflating it with borehole air. The other two are the waste and sampling lines, which run through the bladder and come out the other end. The waste line is larger in diameter than the sample line (3/8" vs. 1/4") to accommodate higher flow rates. At the bottom of the firn hole, the waste line inlet sits about ~10 cm higher than the sample inlet, with the two inlets separated by an aluminum baffle. A high-flow carbon vane pump is used to draw firn air through the waste line. The sample air is drawn by a metal-bellows pump at lower flow rates to ensure cleanliness.

Firn air samples used in COS analysis were collected in 2 L glass flasks with dual glass valves that seal via Teflon o-rings, except for eight replicate NOAA samples from SUM06 that were collected in stainless steel flasks equipped with dual all-metal bellows valves. The two-valve setup enables flushing of the flasks with firn air before collecting the samples. COS samples are from a single firn hole, except SPO08 where samples are from two holes drilled about 30 m apart. The SPO01, SPO08, and MD03 measurements were conducted at NOAA-GML by the HATS group (www.esrl.noaa.gov/gmd/hats/). The SUM13 and REN15 measurements were conducted at the University of California, Irvine (UCI). The SUM06 and SPO15 measurements were conducted at both UCI and NOAA-GML (Table 1).

At NOAA-GML, COS is routinely measured in glass and stainless-steel surface-air flasks collected in pairs for the HATS group as part of their global flask network. Analysis is performed by cryofocusing a barometrically measured volume of dried air onto an uncoated fused silica tube followed by heating-facilitated transfer of trapped gases onto a gas chromatograph with a mass spectrometer detector. COS was detected at ion $m/z = 60^+$. The NOAA-GML measurements are referenced to the NOAA-GML calibration scale that was originally developed in 2004. For more details see Montzka et al. (2004, 2007) and the readme files and updated measurement record (at: ftp://ftp.cmdl.noaa.gov/hats/carbonyl_sulfide/).

At UCI, the firn air samples were analyzed using the same analytical system previously described for ice core air measurements (Aydin et al., 2007, 2008, 2014, 2016). COS is preconcentrated on a glass bead trap (glass beads packed inside an 1/8" stainless steel tube) under vacuum at -196°C . The amount of dry bulk air that has been sampled is determined by a pressure measurement in a temperature-controlled volume located downstream of the trap. The trapped gases are thermally injected into an HP 5890 GC fitted with a DB-1 capillary column (0.25 mm ID, 60 m). The GC is programmed to run through multiple isothermal and temperature ramp-up steps starting at -50°C and ending at 150°C . The GC runs in tandem with a dual focusing magnetic sector mass spectrometer (Waters-Autospec) running at a minimum mass resolution of 8,000 ($m/\Delta m$) in EI + mode.

The UCI measurements are based on detection of the parent COS ion at $m/z = 59.967^+$ ($^{12}\text{C}^{16}\text{O}^{32}\text{S}$). A known amount of ^{13}C labeled COS ($^{13}\text{C}^{16}\text{O}^{32}\text{S}$; $m/z = 60.970^+$) is mixed into every sample during the preconcentration step as an internal standard and used for quantification of the COS in the sample. The isotope-labeled internal standard is calibrated by ppt-level working standards prepared from multiple high concentration (200–300 ppb) primary standards prepared at UCI in 6 L pacified-aluminum tanks (Aculife-Scott Gas). All COS measurements are reported as dry-air mixing ratios, and analytical precision is estimated to be $\pm 1\text{--}2\%$ (1σ).

3. Firn Air Data

The firn at Summit is about 80 m deep, and the full depth was sampled during both the SUM06 and SUM13 campaigns. The SUM06 data include measurements conducted at both UCI and NOAA for 16 sampling depths (Figure 1). The SUM13 samples were analyzed only at UCI, using two different sets of flasks (UCI and NOAA-CCG). SUM13 measurements from a few depths (3 out of 18) were contaminated for multiple trace gases and are not included in the analysis (Hmiel et al., 2020). Renland firn is about 10 m shallower than Summit and frequent surface melting results in the presence of ice lenses throughout the firn column. Two firn holes were sampled during REN15, but the measurements from the first hole were contaminated.

Table 1
Information Relevant for Different Firn Campaigns Included in the Analysis

Site	Firn depth	Inversion period (CE)	No. of sampling depths ^a	Flask origin and type	Analysis location
SUM06	80 m, 1 hole	1907–2006	16	UCI (glass) NOAA (glass and SS)	UCI and NOAA
SUM13	80 m, 1 hole	1914–2013	18	UCI (glass) NOAA-CCG (glass)	UCI
REN15	70 m, 1 hole	1946–2015	12	UCI (glass)	UCI
SPO01	120 m, 2 holes	1802–2001	13 per hole	NOAA (glass)	NOAA
SPO08	117 m, 2 holes	1809–2008	16 per hole	NOAA (glass)	NOAA
SPO15	100 m, 1 hole	1929–2015	8	UCI (glass)	UCI and NOAA
MD03	67 m, 1 hole	1,679–2003	14	NOAA (glass)	NOAA

^aIncludes surface sampling.

Data from 11 out of the 12 sampling depths from the second firn hole are used in our analysis. The deepest Renland sample is not included in the analysis because we have not been able to successfully model the firn air gas age at this depth due to apparent discrepancies between the CH₄, CO₂, and SF₆ measurements.

The air in the top 30–40 m of the firn is influenced by seasonal variability in the overlying atmosphere. From 40 to 65 m, both the SUM06 and SUM13 firn air COS measurements remain at or below 500 ppt (Figure 1).

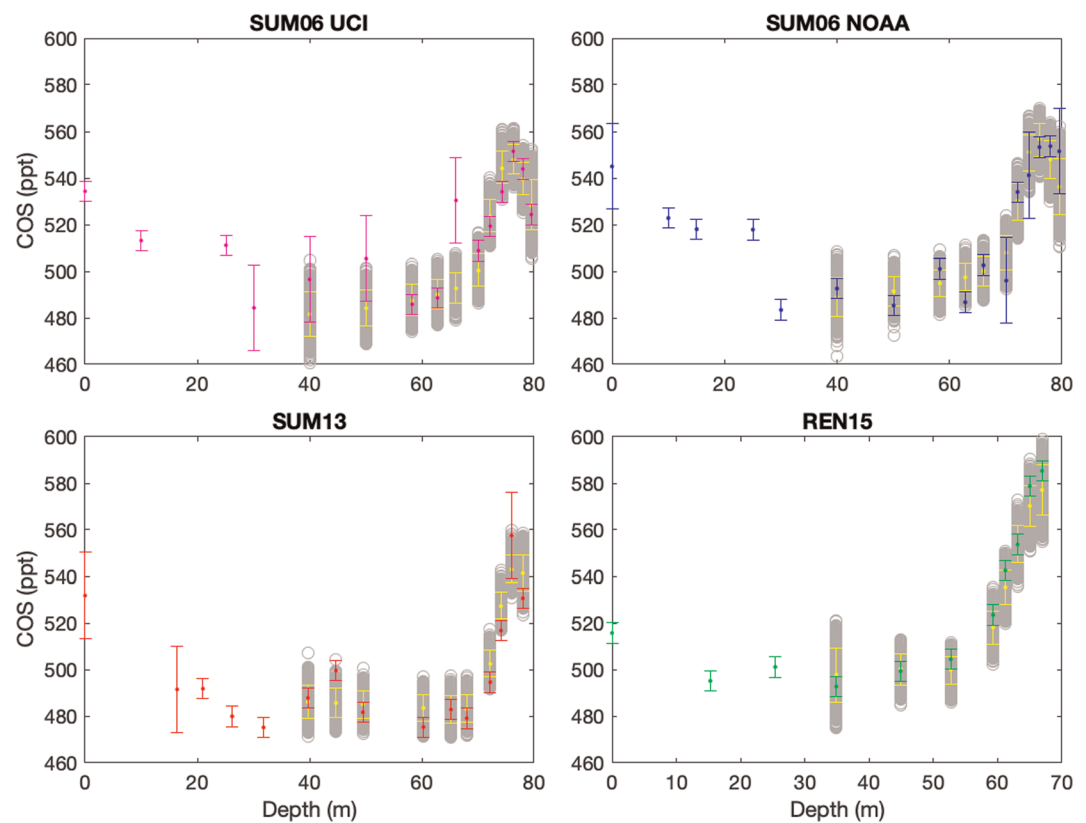


Figure 1. Firn air COS uncertainty estimates ($\pm 1\sigma$) centered around measurement means for Summit and Renland sites in Greenland. SUM06 measurements were conducted at UCI (magenta) and NOAA-GMD (blue) using different sets of flasks. SUM13 (red) and REN15 (green) measurements were conducted at UCI. The gray bands (20,000 circles) represent the firn air COS concentration estimates based on the Bayesian inversion results shown in Figure 7. The yellow error bars represent the 0.025–0.975 quantiles for the gray bands (see section S1 for probability distributions). Only the firn data from below 35 m are included in the inversions to avoid influence from seasonal variability in ambient air. Neither the data nor the inversion results are corrected for gravitational enrichment in the firn.

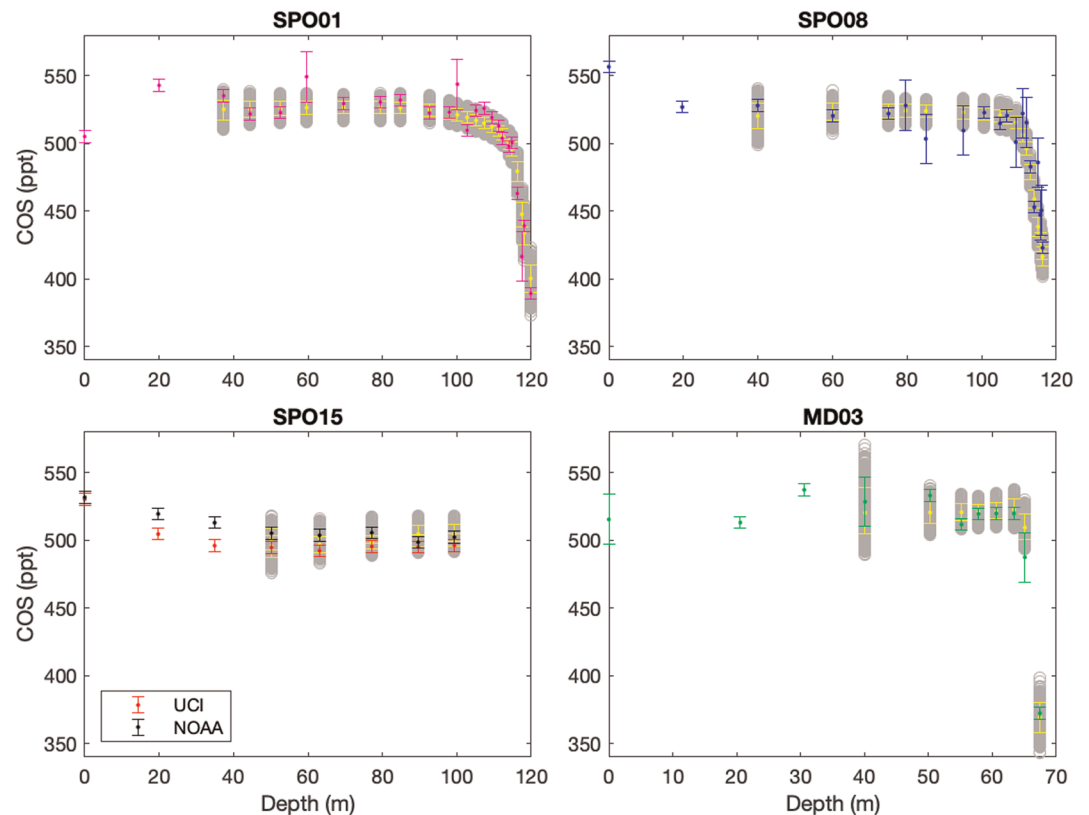


Figure 2. Firn air COS uncertainty estimates ($\pm 1\sigma$) centered around measurement means for the SPO01 (magenta), SPO08 (blue), SPO15 (black and red), and MD03 (green) sites in Antarctica. All Antarctic data are NOAA measurements except one set of SPO15 measurements conducted at UCI (red). The gray bands (20,000 circles) represent the firn air COS concentration estimates based on the Bayesian inversion results shown in Figure 5. The yellow error bars represent the 0.025–0.975 quantiles for the gray bands (see section S1 for probability distributions). Only the firn data from below 35 m are included in the inversions to avoid seasonal variability in ambient air. Neither the data nor the model inversion results shown in this figure are corrected for gravitational enrichment in the firn.

Below 65 m, the COS mixing ratio increases by approximately 10% before leveling off then slightly declining toward the bottom. This basic pattern is present in all firn air COS profiles from Summit. At Renland, a downhole COS increase is also evident from about 50 to 70 m with peak COS levels of about 580 ppt; the basal firn air is younger at Renland than it is at Summit. The firn air COS measurements from all Greenland campaigns point to a period of higher COS in the atmosphere sometime in the recent past.

At the South Pole (SPO), the firn column is close to 120 m thick, with the top 30–40 m under the influence of seasonal variability in surface air and the bubble close-off starting below 100 m (Figure 2). For all SPO campaigns, COS is 500–550 ppt range with no discernable trend down to about 110 m, with a small offset apparent between the SPO15 data from the NOAA and UCI laboratories. Deeper in the SPO firn, there is a steep decline evident in both the SPO01 and SPO08 data, with COS at or below 400 ppt at the bottom of the firn. At Megadunes, the firn is less than 70 m thick, and the bubble close-off zone is confined to below 63 m. The deepest MD03 sample from 67 m measures 372 ppt, which is the lowest COS mixing ratio measured in firn air from any site. It is well established that the basal firn at the South Pole and the Megadunes sites contains older firn air than the Greenland sites (e.g., Battle et al., 1996; Severinghaus et al., 2010). The Antarctic firn air measurements indicate that atmospheric COS levels were much lower than present-day sometime in the beginning of the 20th century or earlier. A precise determination of the timing and the magnitude of atmospheric COS variability based on the firn records requires conducting formal inversions.

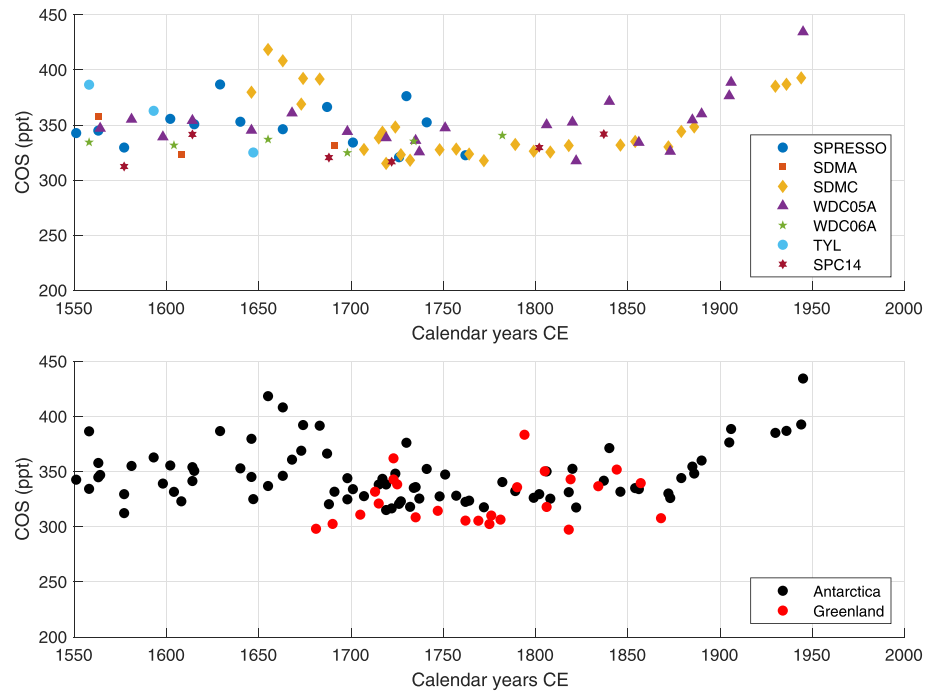


Figure 3. Ice core COS data. (Top) COS data from various Antarctic ice cores ($n = 84$): SPRESSO (South Pole), SDMA (Siple Dome), SDMC (Siple Dome), WDC05A (WAIS Divide), WDC06A (WAIS Divide), TYL (Taylor Dome), and SPC14 (South Pole). Except for the new SPC14 measurements, all data shown here have been published as parts of larger data sets with established chronologies that cover longer periods (Aydin et al., 2002, 2008, 2014; Montzka et al., 2004). The new SPC14 data are on the SP19 chronology (Epifanio et al., 2020). (Bottom) Previously published COS data from the GISP2B and GISP2D ice cores (red circles) from Greenland (Aydin et al., 2007) versus all Antarctic data (black circles) from the top panel.

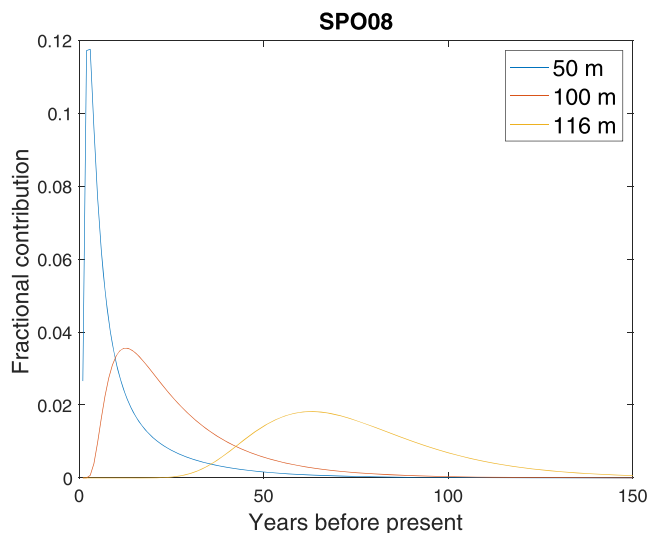


Figure 4. The COS firm air age distribution for the SPO08 campaign at three different depths from the UCI firm model (Aydin et al., 2011). The integral of the age distribution function equals to one at all depths. The smaller amplitude and broader width at depth result in heavier smoothing of atmospheric variability. Slower accumulation sites preserve air with an older mean age, but the older air is also more heavily smoothed. The degree of smoothing at the bottom of the firm is different at each site.

4. Ice Core Data

Previously published ice core COS data sets from Antarctica include measurements from six different ice cores from the Siple Dome, West Antarctic Ice Sheet Divide, and the South Pole sites in Antarctica (Figure 3). In Figure 3, we also present new, previously unpublished measurements from the SPC14 ice core recently drilled at the South Pole as part of the SPICEcore project. All of the ice core COS measurements were made at UCI following published methods and are based on the UCI calibration scale (Aydin et al., 2008, 2014). Temporally overlapping data from different sites agree within uncertainties. The mean of all the Antarctic data is 347 ± 26 ppt ($\pm 1\sigma$). Ice core COS levels are relatively higher and display more variability prior to 1690 CE. During the period that follows, COS remains in the 320–350 ppt range until 1875 CE, after which there is a gradual rise to about 400 ppt by the middle of the 20th century.

The only ice core COS data set from the NH is from a small pilot study, consisting of 25 measurements combined from the GISP2B and GISP2D ice cores drilled at Summit, Greenland (Aydin et al., 2007). The data cover the period from 1681 to 1868 CE, averaging 325 ± 23 ppt ($\pm 1\sigma$) (Figure 3). The overlapping subset of the Antarctic data from 1690 to 1875 CE averages 334 ± 14 ppt ($\pm 1\sigma$). The mean analytical error is estimated to be 12 ± 6 ppt ($\pm 1\sigma$) for the Antarctic measurements and 21 ± 4 ppt ($\pm 1\sigma$) for the

Greenland measurements. The limited temporal extent and the larger errors associated with the Greenland ice core data limit our ability to determine an inter-polar difference.

5. Firn Modeling and Firn Air Age Distribution Functions

The aging of firn gases is closely linked to the rate of firn densification, and it increases nonlinearly with depth. At shallower depths where the ice density is lower than a critical limit ($\sim 800 \text{ kg m}^{-3}$), all porosity in the firn is open (i.e., interconnected). This allows the firn air to mix with the overlying atmosphere at relatively fast rates via molecular diffusion, limiting the aging of gases. At densities higher than 800 kg m^{-3} , open porosity declines, and tortuosity increases rapidly with depth, leading to a quick decline in gas diffusion rates, a fast increase in the gas ages, and a broadening of the age distribution. Firn air transport models are used to determine the aging of gases with depth in the firn. These models commonly include a one-dimensional parameterization of vertical advection and diffusivity as the primary physical processes that control the degree of smoothing in the firn (Battle et al., 2011).

In this study, two 1-D firn air models were used: one developed at UCI and the other at CIC Copenhagen (Aydin et al., 2011; Buizert et al., 2012; Buizert & Severinghaus, 2016; Patterson et al., 2020). The UCI firn air model was used for SPO01, SPO08, and MD03 and has fixed snow accumulation rate and vertically variable diffusion assuming steady-state and isothermal firn. The vertical diffusivity structure is determined empirically by running the model to simulate CO_2 and CFC-12 measured in the firn samples using the known atmospheric histories of these gases. The result of the simulation is compared with the measured CO_2 and CFC-12 firn profiles. The diffusivity parameterization is iteratively adjusted to improve the agreement between simulated and measured firn trace gas profiles. For the MD03 site, the diffusivity tuning of Severinghaus et al. (2010) was used.

The CIC Copenhagen firn air model was used to model SUM06, SUM13, REN15, and SPO15. The CIC model uses a steady-state assumption, isothermal firn, downward advection controlled by the firn porosity, and vertically variable diffusion and dispersion tuned via an automated routine to a suite of several trace gases whose concentrations were measured in the firn air samples and for which the atmospheric history is well known. The model uses the porosity parameterization by Mitchell et al. (2015). For REN15, the steady-state approach should be considered an approximation because gas diffusion rates could be severely impeded over the length of the regularly observed melt layers at Renland.

The vertical diffusivity profiles for both models are adapted to COS using the ratio of the COS molecular diffusivities to the diffusivities of the tune gases. Molecular diffusivities are calculated from empirical relationships (Fuller et al., 1966; Wilke & Lee, 1955). The models generate firn air age distribution functions that characterize the fractional atmospheric contribution from each year in a range of years to the trace gas composition at a given depth in the firn (Figure 4). These age distribution functions are used in the inversions (described in section 6) to infer COS atmospheric histories from the firn air measurements. The repeat campaigns at the same site are treated as individual sites; for example, SUM06 and SUM13 are tuned individually to the atmospheric tracers and have different diffusivity profiles.

6. Bayesian Inversion Framework

A hierarchical Bayesian approach is used to analyze the firn air COS data using the Stan probabilistic software package (mc-stan.org), in which all parameters are interpreted probabilistically and updated using Bayes' theorem according to how consistent the parameters are with the data (Carpenter et al., 2017). The atmospheric mixing ratio (X , ppt) is modeled as an autocorrelated random process (a random walk):

$$X_t \sim N(X_{t-1}, \alpha X_{t-1}), \quad (1)$$

where the probability distribution of X at time step t (X_t) is normally distributed (N) around the mean of X at time step $t-1$ (X_{t-1}) with one standard deviation of αX_{t-1} . The α parameter quantifies how much the atmospheric mixing ratio of COS can change from one year to the next, parameterized as a fraction of the previous year's atmospheric mixing ratio. α can take on a range of values that allow a broad ensemble of different trajectories for X_t , each having a different variance in time. X_t in 1 is evaluated separately for the atmosphere above Antarctica and Greenland.

The measured mixing ratio (M_{mes}) in the firn at a given depth (z) is linked to X by the likelihood function:

$$M_{mes}(z) \sim N\left(\gamma f_{AgeD}(z)X, \beta \sigma_M(z)\right), \quad (2)$$

where the *gamma* (γ) is a constant parameter that accounts for possible offsets between data sets from different sites that may result from calibration differences or other factors (e.g., elevation difference between sites and contamination during sampling), $f_{AgeD}(z)$ is the firn air age distribution function from the firn model specific to every sampling depth at each site, $\sigma_M(z)$ is the measurement error, and *beta* (β) is a constant scalar parameter for the measurement error. All terms in 2 other than X are site specific and treated separately at each individual site. We use one X (X_{GRN}) in all Greenland inversions and another one (X_{ANT}) for all Antarctic inversions, recovering two independent atmospheric histories. The inversion starts with an a priori ensemble of simulations; the posterior distributions are then determined based on the likelihood of the ensemble members given the observations and their uncertainties, following Bayes' theorem (Gelman et al., 2013). All inversions are conducted with the Stan shell interface (CmdStan) Version 2.21.0.

The uncertainty estimates for the measurements are based on reproducibility defined as the standard deviation of measurements from the same depth. The reproducibility can be estimated from repeated measurements of the same flask or from measurements of different flasks filled at the same depth, provided there are multiple flasks from the same depth. For all the firn campaigns, the number of replicate data from a given depth is often limited to two (same flask measured twice or two flasks from the same depth each measured once), which is not sufficient for a good estimate of the standard deviation. When all the error estimates for all depths are evaluated together, we find that the standard deviation of replicate measurements and replicate flasks are the same, except in rare cases where replicate flasks display larger than average standard deviation. We exclude such depths as outliers and calculate an average standard deviation for all depths except the outliers. Outlier depths are also included in the analysis, but with a larger average uncertainty based on the replicate data from outlier depths (Figures 1 and 2). One of the reasons why a β parameter is included in 2 is to compensate for the possibility that the calculated average standard deviation may underestimate the true measurement error arising from uncertainties in the sampling and analysis of firn air.

The inversion model does not explicitly address the potential uncertainty arising from the dimensionless $f_{AgeD}(z)$ term specific to each site. When simultaneously inverting firn data from multiple sites, site-specific errors in the $f_{AgeD}(z)$ should not result in coherent features in the posterior probability distributions of X . However, systematic errors in $f_{AgeD}(z)$ that applies to all Greenland and Antarctic sites can result in features in the posterior distributions that are not real. The β parameter in 2 can also account for errors resulting from f_{AgeD} . If the firn air measurements from different sites are perfectly consistent with the model described by 1 and 2 within the estimated measurement uncertainties, the posterior for β should approximate to 1; otherwise, $\sigma_M(z)$ does not specify the absolute uncertainty.

The number of elements of X is equal to the total number of years included in the inversions, which is 109 years for the Greenland inversion (from 1907 to 2015 CE) and 337 years for the Antarctic inversion (from 1679 to 2015 CE). This total number of years is larger than the number of years constrained by firn air at any of the individual firn sites (periods covered by f_{AgeD} shown in Table 1) because we use data from multiple firn campaigns carried out in different years. An advantage of using data from multiple firn campaigns to constrain one atmospheric history is that the temporal variance between the different campaigns can provide temporal constraints on the inversion over time scales shorter than the time scales of firn smoothing at each individual site.

In 2, data from each firn campaign constrain a different segment of the atmospheric history, but often with considerable overlap. For example, the SUM06 and SUM13 campaigns constrain the Greenland atmospheric history (X_{GRL}) counting 100 years back from 2006 and 2013 CE, respectively, while REN15 data constrain X_{GRL} counting 70 years back from 2015 CE. In the vector multiplication $f_{AgeD}(z)$ times X for each site, we ensure that both factors have the same number of elements by indexing $f_{AgeD}(z)$ into a different segment of X in the code (section S5 in the supporting information).

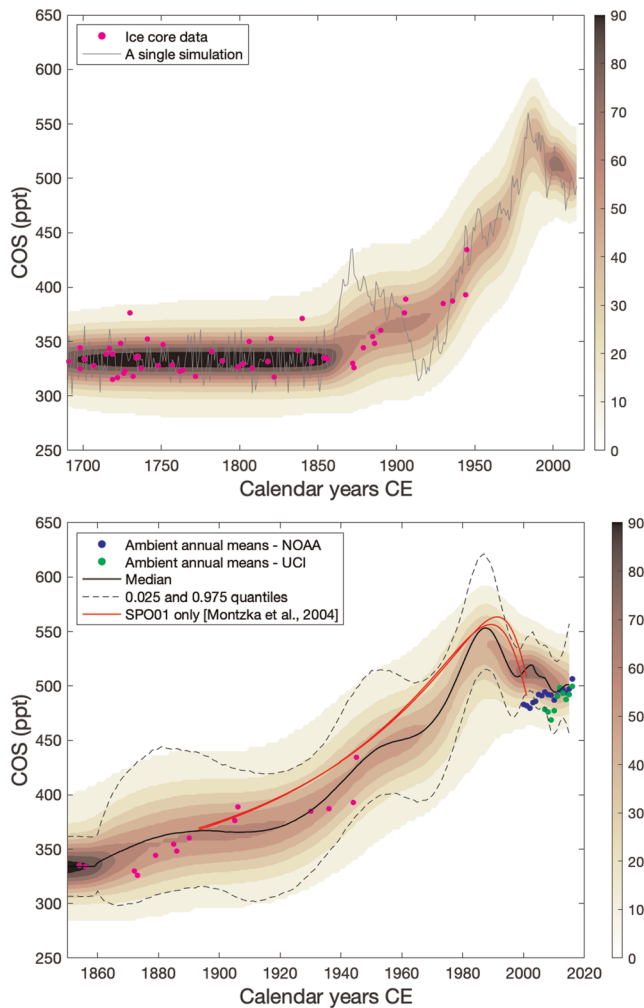


Figure 5. Data density plots (contour plot of histograms) of the Antarctic inversion results, with the resulting firn air concentrations shown in Figure 2 (see section S2 for the full posterior range). The darkest color contours from 1850 to 2015 CE correspond to the periods with highest data density. The darker colors at each year correspond to the concentration range covered by most of the posterior results for that year. (Top) One random simulation of X (gray line) and the Antarctic ice core data (magenta circles) are also shown. Only the ice core data from before 1860 CE are used in the inversion. (Bottom) The same as the top but zoomed into the period after 1855 CE. Also shown are the 0.025, 0.5, and 0.975 quantiles of the X_{ANT} posterior (solid and dashed black lines), the previously published COS atmospheric histories based on the SPO01 firn only (red lines; Montzka et al., 2004), and the ambient air annual means from flasks filled at the SPO and Cape Grim, Australia, measured at NOAA (blue circles) and UCI (green circles).

7. Monte Carlo Sampling and Results

Stan uses fast Hamiltonian MCMC sampling (Carpenter et al., 2017) to draw samples from the joint posterior probability for X and all the other parameters in 1 and 2 that are conditioned on the measured firn air mixing ratios and the estimated measurement uncertainties. Parameters are drawn from uniform prior distributions, which can have prescribed upper and lower bounds, and evaluated for their consistency with the observations via the likelihood function 2. The algorithm iteratively samples the parameters with a frequency proportional to the posterior parameter probability. A total of 5,000 iterations are conducted using four different chains for both the Antarctic and the Greenland inversions. Each chain initializes the search from a different set of randomly drawn parameters. The posterior results include 20,000 iterations total from four different chains.

The inversions are conducted with lower and upper prior bounds of 10–1,500 ppt for X . The α and β parameters are positive by definition with no other restriction on their priors (i.e., $\alpha > 0$ and $\beta > 0$). X draws do not exceed or reach the set bounds of the search, indicating we are not restricting the search by these bounds. The dimensionless site-specific γ parameters are constrained to $a \pm 2\%$ (0.98 to 1.02) range, allowing up to 4% offset between different data sets because we estimate the temporal consistency of the calibration scales to be 3–4% or better. It is possible that the annual mean atmospheric mixing ratio of COS over Renland is somewhat different than it is over Summit because of the elevation difference between the sites, but we do not prescribe a broader prior on the Renland γ parameter. Over Antarctica, any difference in the true atmospheric abundance of COS between SPO and MD is likely small, considering both are East Antarctic sites at similar elevations with no local sources and sinks. The sensitivity of the results to different ranges of γ has been tested. Smaller γ ranges result in larger variability in the inferred atmospheric histories with larger uncertainty estimates; ranges larger than $\pm 2\%$ do not result in smoother atmospheric histories nor do they significantly change the estimated uncertainties (section S3).

7.1. Antarctic Inversions

The Antarctic inversion extends back to 1679 CE due to the long-tailed air age distribution function at the bottom of the Megadunes firn. However, the one MD03 data point from the bottom does not sufficiently constrain the oldest 150–200 years of the Antarctic atmospheric history. Instead, we use the Antarctic ice core measurements from the 1679–1860 CE period (Figure 3) to describe the prior distributions using

$$X_{1679-1860\text{ CE}}^{ANT} \sim N(334 \text{ ppt}, 14 \text{ ppt}), \quad (3)$$

given that the mean and 1 stdev of the ice core data from this period are 334 and 14 ppt. We do not use the ice core data after 1860 CE as a prior because the data display a temporal trend and the temporal resolution is low (Figure 3). Surface air data are not used to constrain the inversions either.

Prior to 1860 CE, the posterior results for the Antarctic atmospheric history of COS (X_{ANT}) remain within the mean and standard deviation prescribed by 3, resulting in tight data densities in posterior atmospheric histories during this period by design (Figure 5). The ice core data from the 1679–1860 CE period are consistent with the deepest data point from MD03 as demonstrated by the simulated firn air COS concentrations at that

depth (gray bands in Figure 2). After 1860 CE, the posterior distributions at each year widen as a result of the fact that ice core data are not used to constrain the inversion anymore and the firn air data only weakly constrain these periods due to the broad age distribution functions for the deepest firn samples. The posterior distributions gradually narrow toward the present day due to the increase in firn air data and narrowing of the age distributions. The regions of densest data and the median of the post-1860 CE posterior distributions are generally consistent with contemporaneous Antarctic ice core data, which have not been included in the inversion, providing further evidence that Antarctic firn air and ice core COS measurements are consistent (Figure 5).

SPO01 firn data have previously been used in a single-site inversion and the two firn-only (not constrained by surface flask measurements) atmospheric histories from Montzka et al. (2004) fall within the 0.025–0.975 quantile (95% confidence) band of the results from the current multisite inversion (Figure 5). The SPO01 firn-only atmospheric histories were based on an inversion with a different firn model output than what has been used here and were reported without formal uncertainty estimates. The ambient air results from both UCI and NOAA also fall within the 95% confidence band of our analysis; this is notable, given that the inversion is not forced to agree with either the instrumental record or the surface samples collected during the firn campaigns. However, the earlier part of the flask record from the 1990s through the early 2000s do not overlap with the highest likelihood (higher data density) region of the posterior results, suggesting a possible discrepancy during this period.

The predominant feature of the Antarctic firn inversions is a rise in COS that starts in the 19th century and continues through most of the 20th century (Figure 5). Since there is no explicit smoothing in the inversion model, short-term variations appear in all individual atmospheric histories. The averaging of 20,000 individual posterior simulations smooths out all higher-frequency variability that is not constrained by the firn air data. Some low-frequency variability is retained as evidenced by two plateaus during the ramp-up period: one from 1890 CE to 1920 CE and the other from 1955 CE to 1965 CE. The steepest COS rise in the record occurs after 1970 CE, culminating in a maximum in the mid-1980s, followed by a period of decline punctuated by a minimum near 2010 CE. The 95% confidence band for the analysis is large early in the 20th century and decreases after 1960 CE until the last few years when it broadens again.

The marginal posterior distributions for the parameters (α , β , and γ) are shown in Figure 6. The α parameter has a skewed distribution with a mean of 0.032 and a median of 0.029, meaning the year-to-year change in the inferred atmospheric mixing ratio of COS averages 3%. Note that the posterior atmospheric histories are consistent with a broad range of α values, with the 0.025 and 0.975 quantiles equal to 0.015 and 0.069 and the minimum and maximum equal to 0.011 and 0.160. The β parameter is more symmetrically distributed with a mean and a median of 1.49 and 1.48 (0.025 and 0.975 quantiles equal 1.20 and 1.86), indicating the 1σ uncertainty estimates for the data were scaled up by about 50% on average during the inversion. Most of the site-specific γ parameters display truncated distributions; the sensitivity of results to broader priors on gamma has been tested and found not to impact the results (section S3). Nearly all the γ draws for the SPO01 and SPO08 campaigns are higher than 1, indicating these data are positively biased with respect to the posterior atmospheric history. In contrast, nearly all the draws for the SPO15 UCI data are lower than 1. The γ distributions for the SPO15 NOAA and MD03 data are more evenly distributed across the prescribed $\pm 2\%$ range and display only very small ($<1\%$) negative biases from the posterior atmospheric histories (Figure 6).

Two plausible causes of offsets between different data sets are calibration offsets between the NOAA and UCI labs and changes in calibration scales over time within both laboratories. It is unlikely production or loss processes in the firn are significant contributing factors because the differences between γ parameters are largest between the different campaigns conducted at the same site and such processes are not expected to introduce a constant bias to the entire data set. Contamination during sampling and chemical production or loss in the flasks can result in apparent offsets between data sets, but the nature of the contamination or the chemical processes has to be such that approximately the same amount of COS must be introduced to or removed from all the flasks from the same campaign.

The inclusion of the γ parameters allows the inversion to converge to a posterior distribution that is less likely to include artifacts resulting from potential biases between the firn data from different campaigns. However, this does not preclude the possibility that the posterior distribution itself is biased with respect

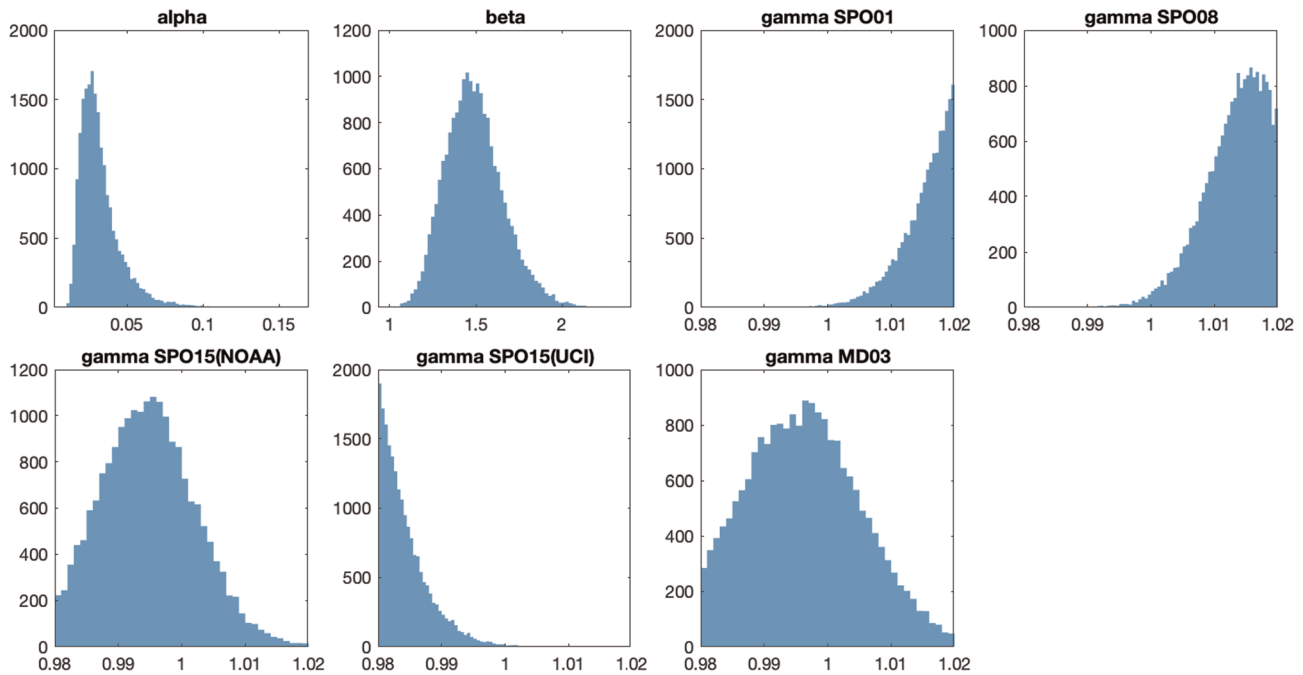


Figure 6. Antarctic posterior probability distributions for the α , β , and the site-specific γ parameters. All γ parameters stay within $\pm 2\%$ of 1 by design. Sensitivity of the results to broader γ ranges has been tested (section S3).

to the real atmosphere. Based on our analysis, the largest bias is between the NOAA SPO01 and the UCI SPO15 data sets (Figure 6). With 89% of the SPO01 γ posteriors higher than 1.01 and 91% of the UCI SPO15 γ posteriors lower than 0.99, there is at least a 2% offset between the data sets from these two campaigns. Note that we cannot determine an upper limit for this offset; however, the upper limit of potential biases between the data sets is rather inconsequential for the posterior distribution of the atmospheric history, as it only slightly augments the uncertainty bounds (section S3).

7.2. Greenland Inversions

The Greenland inversions are conducted for the period from 1907 to 2015 CE. There are no Greenland ice core measurements that can be used to constrain the Greenland inversion. The COS atmospheric history in 1907 CE is prescribed a uniform prior distribution ranging from 200 and 1,000 ppt. The rest of the Greenland atmospheric history (X_{GRN}) is from the joint posterior distribution defined by Equations 1 and 2 using the same priors on α , β , and γ as the ones used in the Antarctic inversions.

Prior to 1940 CE, the posterior range of atmospheric COS is very large and not well constrained as evidenced by very low data density at the peak of the histograms and a broad 95% confidence band around the median (Figure 7). After 1940 CE, the 95% confidence band narrows, and the posterior density is increasingly concentrated around the median, indicating a better constrained inversion. There is a prominent peak in COS mixing ratio that is centered in the mid-1970s CE. The magnitude and timing of this peak is constrained by data from all three Greenland campaigns (Figure 1). After the peak, COS declines by roughly 100 ppt. This decline continues through the 1990s CE, reaching a minimum in 2003 CE.

All annually averaged NOAA surface flask network data from Summit fall within the 95% confidence band even though the surface flask data are not used to constrain the inversion (Figure 7). However, there seems to be a small bias between the firm air reconstruction and the surface flask network data, with most of the flask data lying below the posterior median. The small late peak in the reconstructed atmospheric history after 2010 CE is not evident in the NOAA flask record. To our knowledge, there is no other published formal COS firm inversion from a NH site. The COS data from the Devon Island firm display evidence for a decline in atmospheric COS during the late 20th century (Sturges et al., 2001), which is consistent with the results of our analysis.

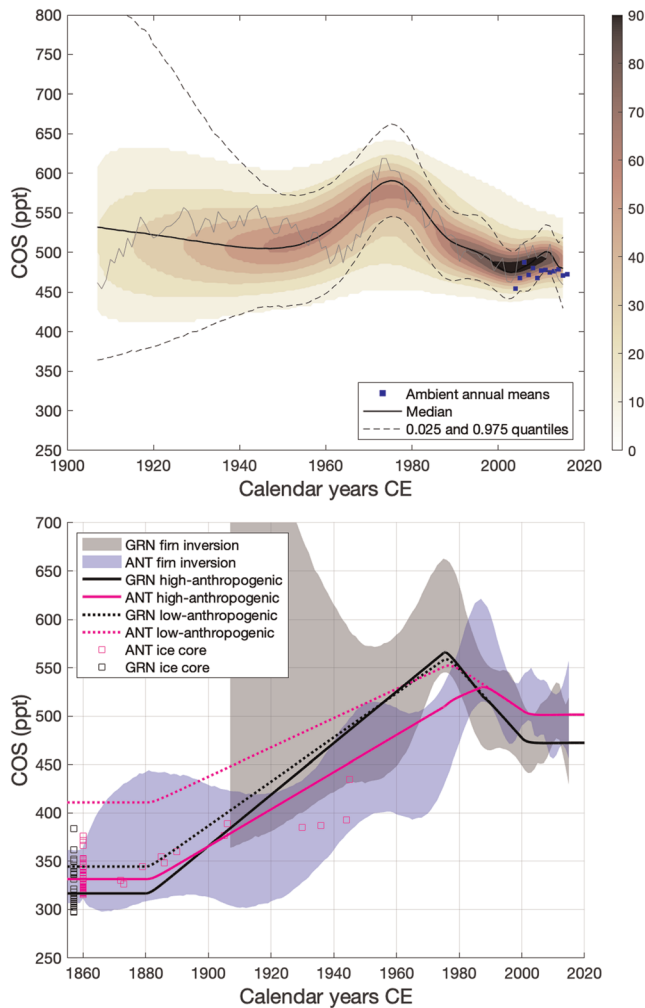


Figure 7. (Top) Data density plots (contour plot of histograms) of the Greenland inversion results, with the resulting firn air concentrations shown in Figure 1 (see section S2 for the full posterior range). Also shown are one random simulation (solid gray line); the 0.025, 0.5, and 0.975 quantiles of the posterior X_{GRN} (solid and dashed black lines); and the ambient air annual means from Summit surface flasks measured at NOAA (blue squares). (Bottom) The 0.025–0.975 quantile range for the Antarctic (blue shade) and Greenland (black shade) inversions compared with the box model high (solid lines) and low (dotted lines) anthropogenic emissions scenarios for Antarctica (magenta) and Greenland (black). The ice core data (Figure 3) from Antarctica (magenta squares) and Greenland (black squares) are also shown, with measurements from before 1860 CE plotted on a collapsed x-axis scale.

in the NH exceeded the SH in the early 20th century, perhaps as a result of anthropogenic emissions. One caveat to this inference is that samples from the base of firn holes can be more prone to contamination during sampling than the samples from shallower depths (Buizert et al., 2012; Hmiel et al., 2020). If this occurred at the bottom of the SUM06 firn hole, the early Greenland inversion results could be biased high with respect to the true atmospheric levels.

For every year from 1907 to 1975 CE, roughly 98% (average over 68 years) of the Greenland posterior atmospheric histories are higher than the median of the Antarctic posterior atmospheric histories, and about 81% are higher than the 0.975 quantile. Therefore, it is likely that COS was higher over Greenland than Antarctica for most of the 20th century, and by extension higher in the NH than in the south. The most

The marginal posterior probability distributions for the Greenland atmospheric history in 1907 CE (first element of the vector X) and for the constant parameters (α , β , and γ) for the inversion are shown in Figure 8. The posterior for the atmospheric mixing ratio in 1907 CE shifted from the uniform prior into a nonuniform skewed posterior, indicating that the firn measurements impose some constraints on the Greenland atmospheric history from as early as 1907 CE. The distribution of the α parameter is slightly skewed with a mean and a median of 0.035 and 0.032, the 0.025 and 0.975 quantiles equal to 0.016 and 0.072, and the minimum and maximum equal to 0.010 and 0.128. The year-to-year change in Greenland COS averages 3%, similar to the Antarctic inversion results. The fact that the posterior α converges to a unimodal distribution with a similar mean state and distribution to the Antarctic inversion is encouraging. This suggests the long-term variations displayed by the inversions from Greenland and Antarctica are representative of real atmospheric changes, rather than processes that are expected to impact the data from different campaigns differently (e.g., production/loss of COS in the firn, sampling issues specific to some campaigns, and inaccuracies in firn model age distribution functions).

The β distribution is minimally skewed with a mean and a median of 1.66 and 1.64 (0.025 and 0.975 quantiles equal 1.26 and 2.21), indicating the 1σ error estimates based on the reproducibility of measurements were scaled up by over 60% on average. The γ parameters for the Greenland inversion are generally truncated. The two data sets from the SUM06 campaign display about 1% negative bias (SUM06 UCI) and 1% positive bias (SUM06 NOAA), respectively. Data from the SUM13 and REN15 campaigns are highly truncated, with most posterior distributions displaying either a 2% negative bias (SUM13) or 2% positive bias (REN15). As noted earlier, the Renland site is at lower elevation than Summit and may experience higher ambient COS levels, although we expect the difference to be small based on comparison of instrumental data from other NH sites within the NOAA network (Montzka et al., 2007).

7.3. Synthesis of Antarctic and Greenland Inversions

The ice core data suggest that preindustrial COS levels over Greenland during the late 1700s CE were not higher than those over Antarctica (Figure 3). The firn air inversions indicate that by the early 20th century, Greenland COS levels were higher than Antarctic levels (Figure 7). About 90% of the Greenland posteriors from 1907 CE are higher than 422 ppt, which is the average 0.975 quantile of the Antarctic posteriors from 1900 to 1920 CE, suggesting the COS levels

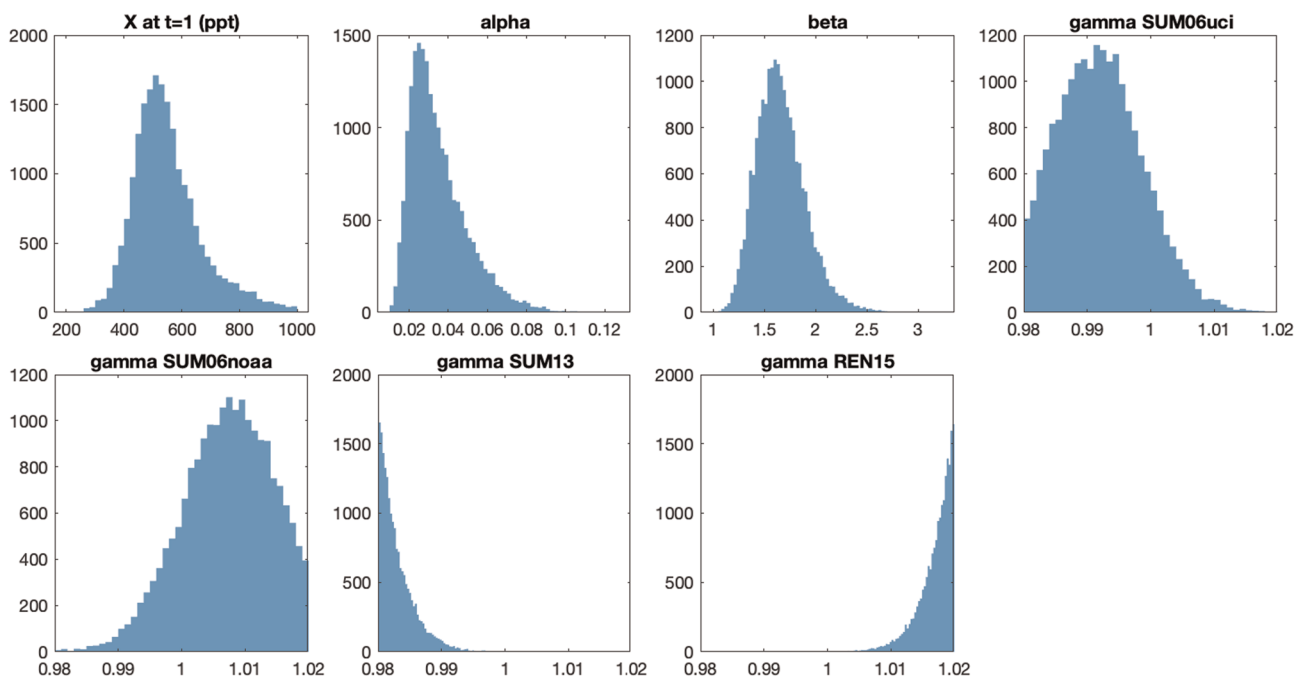


Figure 8. Greenland posterior probability distributions for the α , β , and the site-specific γ parameters, and for the initial atmospheric history (X in 1907 CE). All γ parameters stay within $\pm 2\%$ of 1 by design. Sensitivity of the results to broader γ ranges has been tested (section S3).

notable difference between the records is the timing of the primary COS maxima in the records with the peaks in median posteriors occurring in 1975 and 1987 CE over Greenland and Antarctica, respectively.

In the individual posterior histories from 1950 to 2000 CE, the COS peak occurs in or after 1981 CE in more than 95% of the posterior histories for Antarctica, and it occurs in or before 1980 CE in more than 91% of the posteriors for Greenland. For a lag of 5 years, we find that the COS peak occurs in or after 1984 CE in about 80% of the Antarctic posterior histories and in or before 1979 CE in about 85% of the Greenland ones. After 2010 CE, the COS mixing ratio in both hemispheres remain very close with overlapping uncertainty bands, which is in line with the ambient air results from the NOAA flask network.

To test the possibility that the time lag between the late 20th century atmospheric COS peaks over Greenland and Antarctica may be due to inaccuracies in the firn modeling, we conducted inversions for only the SUM06 campaign using both the UCI and CIC firn models and compared the results to the result presented in section 7.2 (section S4). We do not find any indication that the COS peak over Greenland occurred at the same time as Antarctica. Although this sensitivity test does not address all possible uncertainties in the firn modeling, it suggests that if the time lag between the Greenland and Antarctic atmospheric histories is caused by the inaccuracies in the firn modeling, the possible cause is unlikely to be site specific; rather, it must apply to all or most of the sites.

8. Possible Causes of Atmospheric COS Variability

Antarctic ice core measurements imply that atmospheric COS was 300–350 ppt for several millennia preceding the 20th century (Aydin et al., 2014), constraining the natural background concentrations of atmospheric COS. The general characteristics of the COS atmospheric history over the last 100+ years are suggestive of an emission history dominated by anthropogenic sources as the late 20th century peak is preceded by a large increase and followed by a rapid decline into a relatively stable period in the 21st century (Figures 5 and 7). This pattern is typical for an atmospheric trace gas whose primary emissions are from fossil-fuel production and use, as demonstrated by prior firn air studies of various nonmethane hydrocarbons and carbon monoxide (Aydin et al., 2011; Helmig et al., 2014; Petrenko et al., 2013; Worton et al., 2012). The similarity between the estimates of historical anthropogenic COS emissions and the firn air atmospheric histories

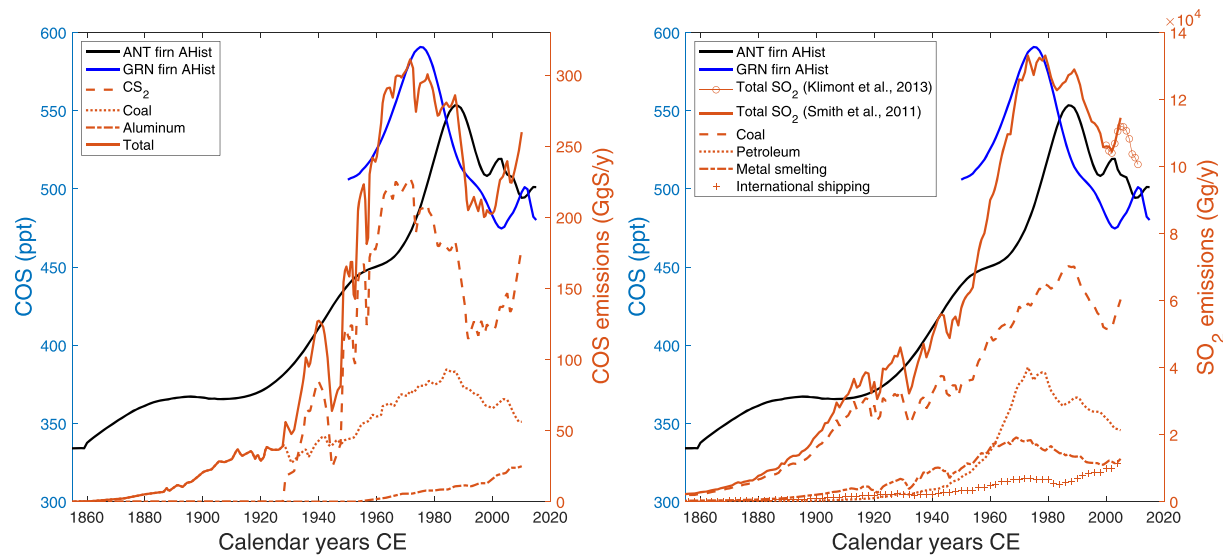


Figure 9. (Left) Median X_{GRN} (blue line) and X_{ANT} (black line) are on the left y axis. The historical anthropogenic COS emissions inventory by Campbell et al. (2015) is on the right y axis. The total inventory emissions (solid red line) is the sum of emissions from CS_2 (dashed line), coal use (dotted line), and aluminum smelting (dashed dotted line). (Right) The same as the left panel but COS emission inventory is replaced with the historical anthropogenic SO_2 inventory by Smith et al. (2011). The major components of the total anthropogenic SO_2 inventory are emissions from petroleum (dashed line), coal (dotted line), metal smelting (dashed dotted line), and shipping (plus sign) sectors. Biomass and biofuel burning emissions are not shown. Emissions from coal are common to both the SO_2 and COS inventories. Metal smelting sector in the SO_2 inventory includes emissions from aluminum smelting, which is the only metal smelting sector accounted for in the COS inventory.

provides further evidence for the dominant influence of anthropogenic emissions in driving the atmospheric COS variability since the 19th century (Figure 9).

Table 2
The Box Model Budget at Tie-Points for the Two Scenarios in $Gg\ S\ year^{-1}$

Sources	1880 CE ^a	1975 CE	1987 CE	2000 CE ^a	B2013
Low anthropogenic emissions					
Ocean (COS)	163	105	114	125	39
Ocean ^b (CS_2 , DMS)	237	237	237	237	237
Balance	515	515	515	515	600 ^c
Anthropogenic ^b	0	500	375	250	180
Biomass burning ^b	70	120	130	136	136
Biofuel burning ^b	10	30	40	40	0
Total	995	1,533	1,417	1,305	1,192
High anthropogenic emissions					
Ocean (COS)	186	117	115	125	
Balance	129	129	129	129	
Balance- anthropogenic	0	129	386	386	
NH anthropogenic	200	190	0	0	
Total anthropogenic ^d	200	819	761	636	
Sinks ^e					
Vegetation + soil	908	1,373	1,301	1,200	1,093
Chemical (OH)	86	127	121	113	101

Note. B2013 COS budget (last column) also shown (Berry et al., 2013).
^aEmissions are flat before 1880 CE and after 2000 CE. ^bAlso valid for the high anthropogenic emissions scenario. ^cAddition to direct ocean COS source suggested by B2013. ^dSum of anthropogenic, balance-anthropogenic, NH anthropogenic sources (see Figure 10). ^eFor the low anthropogenic emissions scenario only, not at steady state.

In this section, we use a coupled atmosphere-surface ocean box model to examine whether the main features of the Greenland and Antarctic atmospheric histories are consistent with the present understanding of the atmospheric COS budget and the bottom-up estimates of historical anthropogenic COS emissions. In the analysis, we assume that the production and loss rates of COS in the oceans as well as the indirect emissions linked to CS_2 and DMS remained constant through time. The changes in burning-related COS emissions are based on existing estimates. We also assume temporally constant rate constants (constant lifetime) for removal of COS from the atmosphere and later discuss the implications of this assumption.

8.1. Atmospheric COS Budget

In earlier budget estimates, atmospheric removal of COS was scaled with net primary productivity (NPP) (Chin & Davis, 1993; Watts, 2000), with model-based top-down estimates converging at 200–300 $Gg\ S\ year^{-1}$ of COS uptake by plants (Kettle et al., 2002). This value roughly matched the observationally constrained estimates of direct and indirect oceanic emissions and resulted in a near-balanced budget with a lifetime close to 4 years (Kettle et al., 2001, 2002). Using data from the NOAA-GML global flask network, Montzka et al. (2007) showed that atmospheric COS exhibited a strong seasonal minimum at NH continental sites that closely followed the summer peak in terrestrial productivity and suggested terrestrial COS uptake should instead be scaled with GPP. Subsequent field and laboratory studies support scaling COS uptake with GPP

of land plants (Campbell et al., 2008; Maseyk et al., 2014; Stimler et al., 2010, 2011; Whelan et al., 2018). This change had the effect of shortening the atmospheric lifetime and increasing the emissions required to balance the budget.

Recent atmospheric modeling-based estimates of the terrestrial COS uptake range from ~ 500 Gg S year⁻¹ (Suntharalingham et al., 2008) to over 800 Gg S year⁻¹ (Berry et al., 2013; Campbell et al., 2017), resulting in a global average lifetime that may be shorter than 2 years. It has been suggested that the larger terrestrial uptake should be balanced by larger oceanic emissions, with modeling-based ocean emission estimates ranging from 800 to 1,000 Gg S year⁻¹ (Berry et al., 2013; Glatthor et al., 2015; Kuai et al., 2015; Launois et al., 2015). In contrast, bottom-up estimates of oceanic COS emissions using direct observational constraints suggest no more than 300–400 Gg S year⁻¹ combined from direct and indirect ocean sources (Lennartz et al., 2017). Present-day anthropogenic emissions, which were estimated at 200–300 Gg S year⁻¹ (Campbell et al., 2015, 2017), are now updated to about 400 Gg S year⁻¹ (Zumkehr et al., 2018), but the source estimates constrained directly by observations still fall short of what is necessary for a balanced budget. The imbalance in the COS budget can result from an incomplete understanding of the existing budget terms and associated uncertainties, or there may be a missing source. The uncertainties notwithstanding, all existing evidence suggests the major terms in the atmospheric COS budget are oceanic (direct and indirect), anthropogenic, and biomass burning emissions on the source side and terrestrial uptake (plant + soil) and chemical oxidation on the sink side (Table 2).

8.2. The Box Model

Atmospheric COS is simulated by a box model that was used for atmospheric ethane (Nicewonger et al., 2016). The atmosphere includes six zonal tropospheric boxes, each representing a 30° latitude band from 90°N to 90°S. Mass exchange between the boxes occurs via annual mean transport parameters calibrated with the global SF₆ distribution (Marik, 1998; Mitchell et al., 2013). The time-dependent COS mixing ratio X in each box is calculated from 5 using the *MATLAB* ode45 fast solver.

$$\frac{dX}{dt} = S(t) - kX(t) + EX(t) \quad (5)$$

In 5, X is the mixing ratio in each atmospheric box, S is the sum of all sources within a box, k is the cumulative pseudo first-order loss rate constant ($k_{OH} + k_{VEG} + k_s$) in a box, and E represents the exchange between neighboring boxes via transport. The sources are described for four tie-points in time (1880, 1975, 1987, and 2000 CE) chosen to capture the main characteristics of the atmospheric COS variability and are linearly interpolated to time steps chosen by the ODE solver. k and E are kept constant over time.

The magnitude of the source terms for each box is prescribed, except the direct COS emissions component of the ocean source is calculated dynamically using a six-box surface ocean model. COS in each surface ocean box equilibrates with the overlying atmospheric box via air/sea gas transfer. Unlike the atmospheric model, there is no exchange between the ocean boxes themselves. The magnitude of the modeled direct ocean COS source is based on the observational estimates for the present-day ocean (Lennartz et al., 2017). COS is produced in the surface ocean by both dark and light processes and lost via hydrolysis and downward mixing. The parameterization of these processes closely follows previous modeling work on ocean-atmosphere exchange of methyl halides (Butler, 1994; Verhulst et al., 2013; Yvon & Butler, 1996). Dark production is set to published values by Lennartz et al. (2017). Photoproduction is tuned to match the magnitude and latitudinal distribution of the present-day direct COS source by Lennartz et al. (2017). Loss to hydrolysis in the surface ocean is calculated from published temperature and pH dependent hydrolysis rates (Elliot et al., 1989; Kamyshny et al., 2003). Air/sea gas transfer is based on the temperature- and salinity-dependent solubility of COS and a surface wind-dependent gas exchange coefficient (Lennartz, 2017). The production terms and the physical parameters that control hydrolysis loss and air/sea gas transfer are assumed to be constant through time. As a result, the ocean acts to buffer the atmosphere against changes in COS due to terrestrial emissions and uptake.

In the troposphere, the major removal mechanisms for COS are uptake by terrestrial vegetation and uptake by soils with first-order rate constants of k_{veg} and k_{soil} , cumulatively accounting for about 90% of model COS loss in the troposphere. k_{soil} is explicitly scaled to be 10% of k_{veg} as recommended by Whelan et al. (2018),

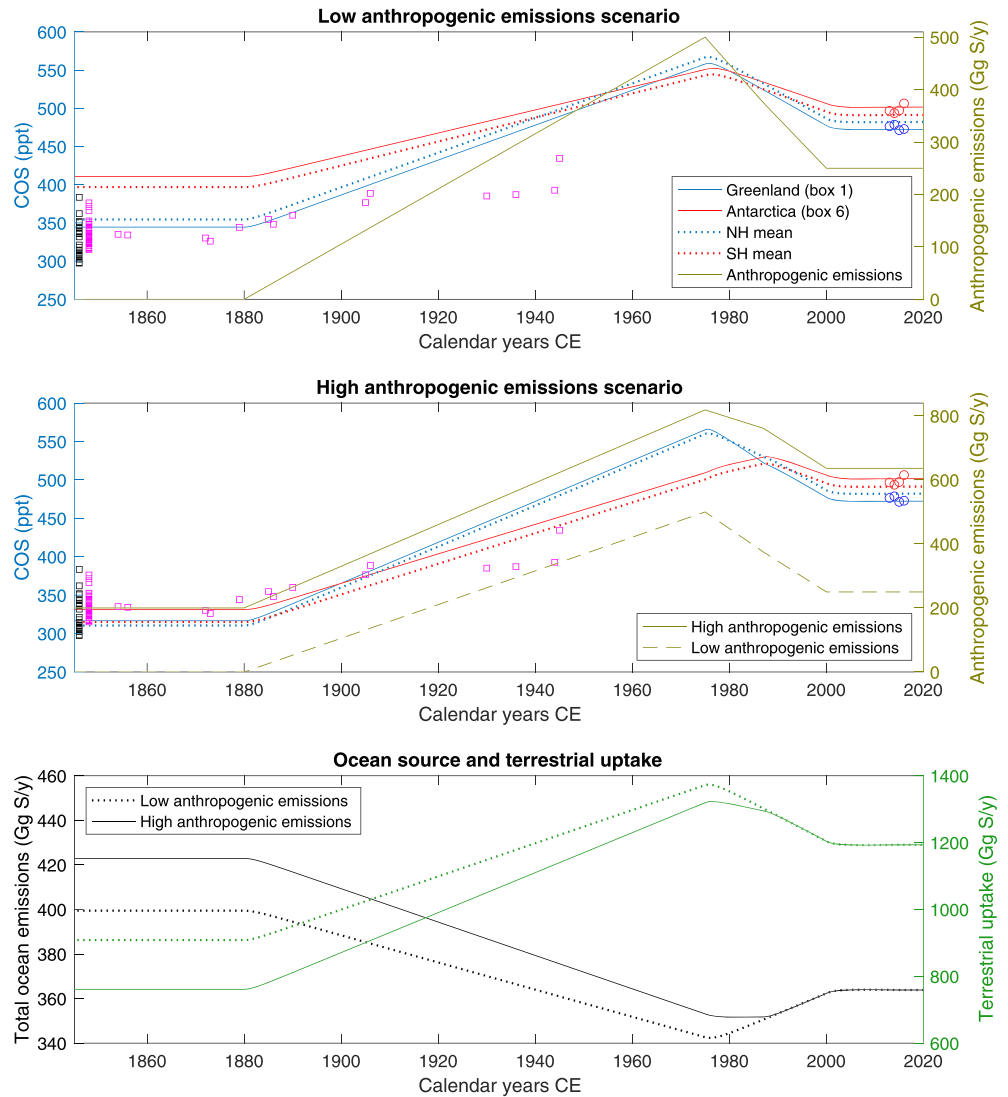


Figure 10. (Top) Low anthropogenic emissions scenario model results. COS over Greenland (blue solid line) and Antarctica (red solid line), in the Northern Hemisphere (blue dotted line) and the Southern Hemisphere (red dotted line) are shown on left y axis along with the ice core data from Antarctica (magenta squares) and Greenland (black squares) and surface flask data from the South Pole (red circles) and Summit, Greenland (blue circles). The ice core data from before 1860 CE are plotted on a collapsed x-axis scale. The total anthropogenic emissions (yellow line) are shown on the right y axis. (Middle) The same as the top panel but for the high anthropogenic emissions scenario. The anthropogenic emissions (solid yellow line) reflect the sum of anthropogenic emissions from the top panel, the part of balance emissions assumed to be of anthropogenic origin, and the NH anthropogenic emissions (Table 2). (Bottom) The total (direct + indirect) net ocean emissions (blue lines) for the low (dotted line) and the high (solid line) anthropogenic emissions scenarios are shown on the left y axis. The total terrestrial (vegetation + soil) uptake (yellow lines) for the low (dotted line) and the high (solid line) anthropogenic emissions scenarios are shown on the right y axis.

although this scaling is inconsequential for the analysis conducted in this work. The magnitude of the cumulative terrestrial uptake rate ($k_{veg} + k_{soil}$) is scaled so that the modeled COS in the present day approximates the observed COS mixing ratios from the NOAA flask network. Chemical loss of COS in the atmosphere occurs via oxidation by OH based on climatological global OH fields (Spivakovsky et al., 2000) and the temperature-dependent rate constant (k_{OH}) (Burkholder et al., 2015). OH oxidation accounts for the remaining 10% of the COS loss in the troposphere. COS loss in the surface ocean also impacts the atmospheric lifetime of COS even though oceans are a large net source (Yvon & Butler, 2002). Other minor loss processes are not included in the model. The tropospheric COS partial lifetimes ($1/k$)

Table 3
Fractional Distribution of Sources (Positive Numbers) and Sinks (Negative Numbers) in the Six Atmospheric Model Boxes

	Box 1 (60– 90°N)	Box 2 (30– 60°N)	Box 3 (0– 30°N)	Box 4 (0– 30°S)	Box 5 (30– 60°S)	Box 6 (60– 90°S)
Ocean COS	0.02	0.45	−0.02	−0.02	0.54	0.03
Ocean CS ₂	0.01	0.10	0.35	0.40	0.13	0.01
Ocean DMS	0.01	0.14	0.23	0.31	0.27	0.04
Balance	0.03	0.05	0.49	0.46	−0.05	0.02
Anthropogenic	0	0.50	0.45	0.05	0	0
Biomass	0.01	0.13	0.31	0.54	0.01	0
Burning ^a						
Biofuel	0.01	0.41	0.38	0.15	0.05	0
burning ^b						
Vegetation ^c	−0.07	−0.33	−0.26	−0.28	−0.06	0
Soil ^d	−0.06	−0.25	−0.32	−0.33	−0.04	0
OH	−0.05	−0.15	−0.31	−0.32	−0.13	−0.04

^avan Aardenne et al. (2001). ^bvan der Werf et al. (2010). ^cPrentice et al. (2011). ^dHashimoto et al. (2015).

with respect to vegetation, soil, and OH sinks are 2.0, 19.3, and 19.8 years, resulting in a globally weighted average lifetime of 1.7 years. The partial lifetime with respect to the ocean uptake in our model is 13.3 years, which lowers the overall lifetime to 1.5 years.

8.3. Implications for Anthropogenic COS Emissions

The COS box model is used to estimate the emission changes required to approximate the major features of the COS variability apparent in the Greenland and Antarctic atmospheric histories. In this analysis, oceanic COS production is kept constant over time, but net emissions can increase or decrease to buffer the changes in atmospheric levels following the mechanism described in section 8.2. The indirect ocean emissions in the form of DMS and CS₂ are constant through time at prescribed levels based on Berry et al. (2013). The biomass and biofuel burning emissions are also prescribed (Berry et al., 2013; Campbell et al., 2017), with minor increases implemented from 1880 CE to 1975 CE for consistency with existing literature (Campbell et al., 2017) (Table 2). By design, the emission changes necessary to drive the atmospheric COS variability are attributed almost entirely to anthropogenic sources defined as industrial activity

and fossil-fuel combustion that are known to emit sulfur containing gases. Two scenarios are explored: (1) low anthropogenic emissions (section 8.3.1) and (2) high anthropogenic emissions (section 8.3.2). The low anthropogenic scenario includes large and temporally constant emissions from an unidentified source to balance the budget, named the “balance” source (Table 2). In the high anthropogenic emissions scenario, a large part of the balance source is temporally varied to better match atmospheric COS changes.

8.3.1. Low Anthropogenic Emissions Scenario

The low anthropogenic emissions scenario is based on the historic and present-day anthropogenic emission estimates from Campbell et al. (2015) and the B2013 global budget assessment, but with a modification to peak emissions as follows. The anthropogenic emissions are set to zero in 1880 CE, increased to 500 Gg S year^{−1} in 1975 CE, lowered to 375 Gg S year^{−1} in 1987 CE, and to 250 Gg S year^{−1} at present (2000 CE onward), linearly interpolating between the tie-points to calculate the annual emissions (Table 2; Figure 10). The historic inventory by Campbell et al. (2015) suggests zero emissions prior to 1880 CE, a peak in the 1970s CE at about 300 Gg S year^{−1}, a drop to about 200 Gg S year^{−1} by 2000 CE, and followed by a rise to 250 Gg S year^{−1} (Figure 9). We use anthropogenic emissions of 500 Gg S year^{−1} in 1975 CE instead of the 300 Gg S year^{−1} suggested in the historic inventory so as to have a pronounced COS peak in the model that more closely resembles the firn air atmospheric histories. The more recent global gridded COS emission histories by Zumkehr et al. (2018) suggest emissions of about 400 Gg S year^{−1} for present day; however, it does not cover the period prior to 1980 CE, and the emission estimates in 1980 CE are the same as present day. The increases in emissions from biofuel and biomass burning from 1880 to 1975 CE (Table 2) contribute to the atmospheric COS rise during the 20th century but constitute a small fraction (<20%) of it.

The geographic distribution of the sources and sinks in the six atmospheric model boxes are shown in Table 3. The balance term in the model (Tables 2 and 3) represents the “missing” COS source attributed to the oceans in B2013. Both the magnitude and the latitudinal distributions of the balance source are calculated to match the magnitude and the distribution of the total direct ocean plus balance sources in the B2013 budget. The difference from B2013 is that we assume that the recent direct ocean source estimate by Lennartz et al. (2017), which is larger than the Kettle et al. (2002) estimates used by B2013, accurately represents the present-day direct ocean COS source. As a result, the balance source in our model is 515 Gg S year^{−1} compared to the 600 Gg S year^{−1} estimate of B2013 (Table 2). We do not assume that the balance source is direct COS emissions from the oceans; rather, it behaves the same way other passive, additive source emissions do (i.e., anthropogenic, indirect ocean, and burning emissions). The negative fraction in Box 5 for the balance source indicates uptake, implying the direct observational estimates are somewhat

larger than the B2013 estimates in this region (Table 3). The negative values for the direct ocean source in Boxes 3 and 4 indicate the ocean acts as a small net sink over this region at present day.

The resultant COS history for the low anthropogenic emissions scenario captures the general characteristics of the observed variability, but with some notable shortcomings (Figures 7 and 10). The COS levels over Antarctica in the 19th century atmosphere are too high compared with the ice core and firn air records, with Antarctica exceeding Greenland by more than 50 ppt. The Antarctic levels stay higher than Greenland during most of the ramp-up period. The model COS peaks in the two hemispheres are only 1 year apart in contrast to the observations that suggest a larger time lag with Greenland leading Antarctica.

8.3.2. High Anthropogenic Emissions Scenario

Assuming that anthropogenic emissions are driving the long-term changes in atmospheric COS, the only way to lower both the Antarctic levels and the inter-polar difference during the 19th century is to (1) introduce anthropogenic emissions during the 19th century in the NH to bring Greenland and Antarctic levels closer together and (2) change the geographic distribution of present-day anthropogenic emissions by increasing the fractional contribution from low-latitude anthropogenic sources so that when they are removed, the COS levels will be lower over both Greenland and Antarctica at the end of the 19th century (Figures 7 and 10). This is done by introducing a new NH anthropogenic source that is additive to those in the low anthropogenic emissions scenario and by gradually increasing the balance source to its present-day level instead of keeping it temporally constant as we did in the low anthropogenic emissions scenario.

The new NH anthropogenic source is emitted from 30–60°N (in Box 2) and set at 200 Gg S year⁻¹ in 1880 CE, decreased to 190 Gg S year⁻¹ in 1975 CE and zeroed in 1987 CE (Table 2). The balance emissions are set to 25% of their present-day value in 1880 CE (129 Gg S year⁻¹), to 50% in 1975 CE (258 Gg S year⁻¹), and to 100% (515 Gg S year⁻¹) in 1987 CE. This means that 75% of the present-day balance emissions (386 Gg S year⁻¹) are introduced during the period from 1880 to 1987 CE and are presumed to be of anthropogenic origin. The total anthropogenic emissions increase from about 200 Gg S year⁻¹ at the end of the 19th century to over 800 Gg S year⁻¹ during the 20th century peak before dropping to 600 Gg S year⁻¹ level at present (Table 2; Figure 10). Note that the magnitude of the emission changes introduced here is considerably larger than the observationally constrained individual ocean sources and biomass burning, suggesting it is unlikely they are natural in origin. This is consistent with long-term ice core records of COS, which show that natural variability of atmospheric COS during the several thousand years preceding the industrial era has been an order of magnitude smaller than the increase during the 20th century (Aydin et al., 2014, 2016).

The high anthropogenic emissions scenario successfully reproduces the main features of the observed COS variability over Greenland and Antarctica (Figures 7 and 9). The lower inter-polar gradient in the 19th century is achieved by introducing anthropogenic emissions in the middle- to high-latitude NH. The time lag between peaks over Greenland and Antarctica is driven by a shift in anthropogenic sources from high northern latitudes to low latitudes in both hemispheres that takes place between 1975 and 1987 CE. Note that the anthropogenic emissions are always predominantly in the NH. The present-day emissions in the high anthropogenic emissions scenario are less than 20% lower than the peak emissions, suggesting anthropogenic emissions at present can be only marginally lower than peak emissions during the 20th century. In the low anthropogenic emissions scenario, the present-day anthropogenic emissions are at 50% of the peak emissions (Figure 10).

8.3.3. Anthropogenic COS Sources

The box model results show that the anthropogenic emissions in the COS historic inventory (Campbell et al., 2015) generally fall short of reproducing the observed atmospheric COS variability and are insufficient to push atmospheric COS to the peak levels observed during the 1970s and 1980s CE. We interpret this as evidence that the anthropogenic emissions are underestimated throughout the 20th century, provided the tropospheric lifetime of COS remained constant during this period. Despite not including enough emissions, the COS historic inventory closely matches the temporal evolution of the peak in atmospheric COS during the 20th century (Figure 9), suggesting there is either an underestimate of emissions from the known anthropogenic sources of COS or there are unidentified anthropogenic sources with emission histories similar to the known sources.

Montzka et al. (2004) noted that the atmospheric history of COS during the 20th century resembles historical anthropogenic sulfur dioxide (SO₂) emissions. Despite including emissions from a larger variety of sources compared to the COS inventory, the SO₂ inventory (Smith et al., 2011) also closely follows the atmospheric changes in COS during the 20th century, displaying double peaks during the 1970s and 1980s CE at exactly the same time as the COS peaks over Greenland and Antarctica occur (Figure 9). The first of the SO₂ emission peaks is linked to maximum emissions from the petroleum and metal smelting sectors while the second one is primarily due to peaking coal emissions. The single broad peak in the COS emission inventory is largely due to CS₂ emissions while the coal emissions are not large enough to cause a secondary peak in the 1980s. The box model results show that the longer than 1 year time lag between the peaks in the Greenland and Antarctic firn COS histories can be caused by geographic relocation of NH sources. The late 20th century is a time period when sulfur mitigation policies were enacted in North America and Europe and emissions started to shift first toward East and South Asia, and later to India, Indonesia, and various locations in South Africa and South America (Klimont et al., 2013; Smith et al., 2011; Stern, 2005).

While there is qualitative evidence that the anthropogenic sources of SO₂ also influence atmospheric COS levels, the coal sector is the only common major source between the SO₂ and COS anthropogenic emission inventories. The most recent bottom-up analysis by Zumkehr et al. (2018) estimates significantly larger COS emissions from coal at present day than the earlier historical inventory by Campbell et al. (2015). Our analysis supports this assessment. We also suggest that the reasons behind entirely omitting the other major SO₂ emitting industries from the COS emission inventories should be reexamined. This might be especially important for periods prior to implementation of regulatory restrictions on use of sulfur containing fuels and sulfur emissions. Coemissions of COS from all major SO₂ emitting industrial sectors might be the only viable explanation for peak anthropogenic COS emissions on the order of 800 Gg S year⁻¹ during the 20th century as implied by our top-down analysis.

8.4. Implications of a Constant COS Lifetime

In the modeling analyses presented in the previous sections, we assumed a constant tropospheric COS lifetime ($1/k$) based on the contemporary understanding of the atmospheric COS budget and the absence of clear evidence that lifetime has varied. Here, we briefly discuss the implications of assuming a fixed COS atmospheric lifetime, focusing on k_{veg} and ignoring possible changes in k_{OH} , k_{soil} , and loss rate constant in the surface ocean.

The assumption of a constant k_{veg} does not necessarily imply that GPP itself remained constant. Stimler et al. (2010) proposed the following relationship between GPP (mol C year⁻¹) and COS uptake (mol COS year⁻¹) based on laboratory chamber studies:

$$COS\ uptake = GPP \times \frac{[COS]}{[CO_2]} \times LRU, \quad (6)$$

where $[COS]$ and $[CO_2]$ are atmospheric mixing ratios of the respective trace gases and LRU is dimensionless normalized leaf relative uptake of COS to CO₂. By substituting COS uptake with k_{veg} (year⁻¹) times the atmospheric mixing ratio of COS, 6 can be rearranged:

$$k_{veg} = \frac{GPP \times LRU}{[CO_2]} \times \frac{1}{mAtm}, \quad (7)$$

where $mAtm$ is the number of moles of air in the atmosphere added for dimensional consistency. Equation 7 implies that the product of GPP and LRU will always scale linearly with atmospheric CO₂ levels if k is constant. This implies large increases in $GPP \times LRU$ since the 19th century given the atmospheric CO₂ rise during this period.

In other words, both the low and high anthropogenic emissions scenarios in sections 8.3.1 and 8.3.2 imply an increase in $GPP \times LRU$ of more than 30% from the 19th century to 2000 CE due to CO₂ increasing from 280 to 370 ppm, and an increase of about 45% through 2020 CE for an atmospheric CO₂ mixing ratio of 410 ppm. LRU is a leaf-scale parameter that might not have varied much over the last several decades (Campbell et al., 2017), implying most or all of this inferred change can be attributed to the GPP. The 30% plus

increase in inferred GPP by 2000 CE agrees with the recent analysis of Campbell et al. (2017). They show that the roughly 30% GPP increase during the 20th century is close to the high-end estimates from the carbon-cycle models. An additional 15% increase in inferred $GPP \times LRU$ since 2000 CE under a constant lifetime assumption and based on 7 has yet to be evaluated against carbon-cycle models.

9. Conclusions

We conducted a simultaneous multisite inversion of firn air data from Greenland and Antarctica for the first time. The Bayesian framework implemented within the Stan statistical programming language is an efficient method for the inversion of firn air measurements to recover atmospheric histories, allowing quantification of uncertainties arising from sampling and measurement errors as well as addressing possible biases between different data sets that may stem from temporal variability in calibration scales applied to COS measurements. We find that these uncertainties are about an order of magnitude smaller than the long-term changes in the atmospheric history of COS. This method can be expanded in the future to quantify the source and sink changes required to explain the inferred atmospheric variability along with the associated uncertainties within a hierarchical Bayesian framework.

Our analysis provides an atmospheric history of COS from Antarctica since the 19th century, constrained by either the ice core or firn air measurements through the length of the record. The Greenland atmospheric history covers most of the 20th century though there is still a 100 year gap between the oldest periods well constrained by the firn air and the youngest ice core measurements. This gap could be closed in the future by shallow ice core measurements. Both the Greenland and Antarctic records suggest a large COS increase in the atmosphere through the first 70–80 years of the 20th century, followed by a decline leading into a relatively stable period near present-day levels. There is strong evidence that the changes in atmospheric COS did not occur in a smooth and monotonic fashion, and it is likely that the peak levels were reached at different times in the two hemispheres, with the NH leading the south.

Model simulations are consistent with the changes in anthropogenic emissions being the primary driver of atmospheric COS variability from the late 19th century to present day. The total anthropogenic emissions required to simulate the COS rise over the past century are larger than existing bottom-up estimates. We suggest that some industrial sectors that are sources of SO_2 but not of COS should be considered to be included in the COS inventories. It is likely that coemissions of COS from industrial sulfur gas emitting sectors are larger than previously thought and changes in the latitudinal distribution of anthropogenic emissions have had an impact on observed COS levels in the polar atmosphere over Greenland and Antarctica. A chemical transport modeling framework is needed to formally determine the historic variability in the anthropogenic COS emissions and their locations. Such work would benefit from independent information on GPP variability to constrain potential changes in the COS lifetime.

Acknowledgments

We thank Todd Sowers and Trevor Popp for the SPO15 and Jeff Severinghaus for the MD03 firn campaigns. We also thank all the drillers and the field support personnel that contributed to the firn air and ice core campaigns. This research was supported by the National Science Foundation Grants ANT-1443470 and ANT-1443472, the U.S. Department of Energy Grant DE-SC0016539, and Simons Foundation Postdoctoral Fellowship in Marine Microbial Ecology. Firn air data (Figures 1 and 2; F1section S6) are archived (under DOI: 10.7289/V51N7ZDK) and can be accessed online (via the following landing page: <https://www.ncei.noaa.gov/metadata/geoportal/rest/metadata/item/gov.noaa.ncdc%3AC01555/html>). The 20,000 COS atmospheric histories from the inversions (Figures S8 and S9) can be accessed as Data Sets S1 (Greenland) and S2 (Antarctica).

References

- Arsene, C., Barnes, I., Becker, K. H., & Mocanu, R. (2001). FT-IR product study on the photo oxidation of dimethyl sulphide in the presence of NO_x -temperature dependence. *Atmospheric Environment*, 35(22), 3769–3780. [https://doi.org/10.1016/S1352-2310\(01\)00168-6](https://doi.org/10.1016/S1352-2310(01)00168-6)
- Asaf, D., Rotenberg, E., Tatarinov, F., Dicken, U., Montzka, S. A., & Yakir, D. (2013). Ecosystem photosynthesis inferred from measurements of carbonyl sulphide flux. *Nature Geoscience*, 6(3), 186–190. <https://doi.org/10.1038/ngeo1730>
- Aydin, M., Campbell, J. E., Fudge, T. J., Cuffey, K. M., Nicewonger, M. R., Verhulst, K. R., & Saltzman, E. S. (2016). Changes in atmospheric carbonyl sulfide over the last 54,000 years inferred from measurements in Antarctic ice cores. *Journal of Geophysical Research: Atmospheres*, 121, 1943–1954. <https://doi.org/10.1002/2015JD024235>
- Aydin, M., De Bruyn, W. J., & Saltzman, E. S. (2002). Preindustrial atmospheric carbonyl sulfide (OCS) from an Antarctic ice core. *Geophysical Research Letters*, 29(9), 1359. <https://doi.org/10.1029/2002GL014796>
- Aydin, M., Fudge, T. J., Verhulst, K. R., Nicewonger, M. R., Waddington, E. D., & Saltzman, E. S. (2014). Carbonyl sulfide hydrolysis in Antarctic ice cores and an atmospheric history for the last 8,000 years. *Journal of Geophysical Research: Atmospheres*, 119, 8500–8514. <https://doi.org/10.1002/2014JD021618>
- Aydin, M., Verhulst, K. R., Saltzman, E. S., Battle, M. O., Montzka, S. A., Blake, D. R., et al. (2011). Recent decreases in fossil-fuel emissions of ethane and methane derived from firn air. *Nature*, 476(7359), 198–201. <https://doi.org/10.1038/nature10352>
- Aydin, M., Williams, M. B., & Saltzman, E. S. (2007). Feasibility of reconstructing paleoatmospheric records of selected alkanes, methyl halides, and sulfur gases from Greenland ice cores. *Journal of Geophysical Research*, 112, D07312. <https://doi.org/10.1029/2006JD008027>
- Aydin, M., Williams, M. B., Tatum, C., & Saltzman, E. S. (2008). Carbonyl sulfide in air extracted from a South Pole ice core: A 2000 year record. *Atmospheric Chemistry and Physics*, 8(24), 7533–7542. <https://doi.org/10.5194/acp-8-7533-2008>
- Battle, M., Bender, M., Sowers, T., Tans, P. P., Butler, J. H., Elkins, J. W., et al. (1996). Atmospheric gas concentrations over the past century measured in air from firn at the South Pole. *Nature*, 383(6597), 231–235. <https://doi.org/10.1038/383231a0>

- Battle, M., Severinghaus, J. P., Sofen, E. D., Plotkin, D., Orsi, A. J., Aydin, M., et al. (2011). Controls on the movement and composition of firm air at the West Antarctic Ice Sheet Divide. *Atmospheric Chemistry and Physics*, *11*(21), 11,007–11,021. <https://doi.org/10.5194/acp-11-11007-2011>
- Berry, J., Wolf, A., Campbell, J. E., Baker, I., Blake, N., Blake, D., et al. (2013). A coupled model of the global cycles of carbonyl sulfide and CO₂: A possible new window on the carbon cycle. *Journal of Geophysical Research: Biogeosciences*, *118*, 842–852. <https://doi.org/10.1002/jgrg.20068>
- Brühl, C., Lelieveld, J., Crutzen, P. J., & Tost, H. (2012). The role of carbonyl sulphide as a source of stratospheric sulphate aerosol and its impact on climate. *Atmospheric Chemistry and Physics*, *12*(3), 1239–1253. <https://doi.org/10.5194/acp-12-1239-2012>
- Buizert, C., & Severinghaus, J. P. (2016). Dispersion of deep polar firm driven by synoptic-scale surface pressure variability. *The Cryosphere*, *10*(5), 2099–2111. <https://doi.org/10.5194/tc-10-2099-2016>
- Buizert, C. P., Martinerie, P., Petrenko, V., Severinghaus, J. P., Trudinger, C. M., Witrant, E., et al. (2012). Gas transport in firm: Multiple-tracer characterization and model intercomparison for NEEM, Northern Greenland. *Atmospheric Chemistry and Physics*, *12*(9), 4259–4277. <https://doi.org/10.5194/acp-12-4259-2012>
- Burkholder, J. B., Sander, S. P., Abbatt, J., Barker, J. R., Huie, R. E., Kolb, C. E., et al. (2015). Chemical kinetics and photochemical data for use in atmospheric studies, Evaluation No. 18, JPL Publication 15-10, Jet Propulsion Laboratory, Pasadena, 2015 <http://jpldataeval.jpl.nasa.gov>
- Butler, J. (1994). The potential role of the ocean in regulating atmospheric CH₃Br. *Geophysical Research Letters*, *21*(3), 185–188. <https://doi.org/10.1029/94GL00071>
- Campbell, J. E., Berry, J. A., Seibt, U., Smith, S. J., Montzka, S. A., Launois, T., et al. (2017). Large historical growth in global terrestrial gross primary production. *Nature*, *544*(7648), 84–87. <https://doi.org/10.1038/nature22030>
- Campbell, J. E., Carmichael, G. R., Chai, T., Mena-Carrasco, M., Tang, Y., Blake, D. R., et al. (2008). Photosynthetic control of atmospheric carbonyl sulfide during the growing season. *Science*, *322*(5904), 1085–1088. <https://doi.org/10.1126/science.1164015>
- Campbell, J. E., Whelan, M. E., Seibt, U., Smith, S. J., Berry, J. A., & Hilton, T. W. (2015). Atmospheric carbonyl sulfide from anthropogenic activity: Implications for carbon cycle constraints. *Geophysical Research Letters*, *42*, 3004–3010. <https://doi.org/10.1002/2015GL063445>
- Carpenter, B., Gelman, A., Hoffman, M., Lee, D., Goodrich, B., Betancourt, M., et al. (2017). Stan: A probabilistic programming language. *Journal of Statistical Software*, *76*, 1–32. <https://doi.org/10.18637/jss.v076.i01>
- Chin, M., & Davis, D. D. (1993). Global sources and sinks of OCS and CS₂ and their distributions. *Global Biogeochemical Cycles*, *7*(2), 321–337. <https://doi.org/10.1029/93GB00568>
- Chin, M., & Davis, D. D. (1995). A reanalysis of carbonyl sulfide as a source of stratospheric background sulfur aerosol. *Journal of Geophysical Research*, *100*(D5), 8993–9006. <https://doi.org/10.1029/95JD00275>
- Crutzen, P. (1976). Possible importance of CSO for sulfate layer of stratosphere. *Geophysical Research Letters*, *3*(2), 73–76. <https://doi.org/10.1029/GL003i002p00073>
- Elliot, S., Lu, E., & Sherwood Rowland, F. (1989). Rates and mechanisms for the hydrolysis of carbonyl sulfide in natural waters. *Environmental Science & Technology*, *23*, 456–461
- Epifanio, J. A., Brook, E. J., Buizert, C., Edwards, J., Sowers, T. A., Kahle, E. C., et al. (2020). The SP19 chronology for the South Pole Ice Core—Part 2: Gas chronology, delta-age, and smoothing of atmospheric records. *Clim. Past Diss.*, <https://doi.org/10.5194/cp-2020-71>
- Fuller, E. N., Schettler, P. D., & Giddings, J. C. (1966). A new method for prediction of binary gas-phase diffusion coefficients. *Industrial and Engineering Chemistry*, *58*(5), 18–27. <https://doi.org/10.1021/ie50677a007>
- Gelman, A., Carlin, J. B., Stern, H. S., Dunson, D. B., Vehtari, A., & Rubin, D. B. (2013). *Bayesian Data Analysis*. London: Chapman & Hall/CRC. <https://doi.org/10.1201/b16018>
- Gimeno, T. E., Ogée, J., Royles, J., Gibon, Y., West, J. B., Burlett, R., et al. (2017). Bryophyte gas-exchange dynamics along varying hydrations status reveal a significant carbonyl sulphide (COS) sink in the dark and COS source in the light. *New Phytologist*, *215*(3), 965–976. <https://doi.org/10.1111/nph.14584>
- Glatthor, N., Höpfner, M., Baker, I. T., Berry, J., Campbell, J. E., Kawa, S. R., et al. (2015). Tropical sources and sinks of carbonyl sulfide observed from space. *Geophysical Research Letters*, *42*, 10,082–10,090. <https://doi.org/10.1002/2015GL066293>
- Goldan, P. D., Kuster, W. C., & Fehsenfeld, F. C. (1988). Uptake of COS by growing vegetation: A major tropospheric sink. *Journal of Geophysical Research*, *93*(D11), 186–192
- Hashimoto, S., Cavvalhais, N., Ito, A., Migliavacca, M., Nishina, K., & Reichstein, M. (2015). Global spatiotemporal distribution of soil respiration modeled using a global database. *Biogeosciences*, *12*(13), 4121–4132. <https://doi.org/10.5194/bg-12-4121-2015>
- Helmig, D., Petrenko, V., Martinerie, P., Witrant, E., Röckmann, T., Zuiderweg, A., et al. (2014). Reconstruction of Northern Hemisphere 1950–2010 atmospheric non-methane hydrocarbons. *Atmospheric Chemistry and Physics*, *14*(3), 1463–1483. <https://doi.org/10.5194/acp-14-1463-2014>
- Hmiel, B., Petrenko, V. V., Dyonisius, M. N., Buizert, C., Smith, A. M., Place, P. F., et al. (2020). Preindustrial ¹⁴CH₄ indicates greater anthropogenic fossil CH₄ emissions. *Nature*, *578*(7795), 409–412. <https://doi.org/10.1038/s41586-020-1991-8>
- Kamyshny, A., Goifman, A., Rizkov, D., & Lev, O. (2003). Formation of carbonyl sulfide by the reaction of carbon monoxide and inorganic polysulfides. *Environmental Science & Technology*, *37*(9), 1865–1872. <https://doi.org/10.1021/es0201911>
- Kesselmeier, J., & Merk, L. (1993). Exchange of carbonyl sulfide (COS) between agricultural plants and the atmosphere: Studies on the deposition of COS to peas, corn and rapeseed. *Biogeochemistry*, *23*(1). <https://doi.org/10.1007/BF00002922>
- Kettle, A. J., Kuhn, U., von Hobe, M., Kesselmeier, J., & Andreae, M. O. (2002). Global budget of atmospheric carbonyl sulfide: Temporal and spatial variations of the dominant sources and sinks. *Journal of Geophysical Research*, *107*(D22), 4658. <https://doi.org/10.1029/2002JD002187>
- Kettle, A. J., Rhee, T. S., von Hobe, M., Poulton, A., Aiken, J., & Andreae, M. O. (2001). Assessing the flux of different volatile sulfur gases from the ocean to the atmosphere. *Journal of Geophysical Research*, *106*(D11), 12,193–12,209. <https://doi.org/10.1029/2000JD900630>
- Kjellström, E. (1998). A three-dimensional global model study of carbonyl sulfide in the troposphere and the lower stratosphere. *Journal of Atmospheric Chemistry*, *29*(2), 151–177. <https://doi.org/10.1023/A:1005976511096>
- Klimont, Z., Smith, S. J., & Cofala, J. (2013). The last decade of global anthropogenic sulfur dioxide: 2000–2011 emissions. *Environmental Research Letters*, *8*(1), 014003. <https://doi.org/10.1088/1748-9326/8/1/014003>
- Kuai, L., Worden, J. R., Campbell, J. E., Kulawik, S. S., Li, K. F., Lee, M., et al. (2015). Estimate of carbonyl sulfide tropical oceanic surface fluxes using Aura Tropospheric Emission Spectrometer observations. *Journal of Geophysical Research: Atmospheres*, *120*, 11,012–11,023. <https://doi.org/10.1002/2015JD023493>

- Lana, A., Bell, T. G., Simo, R., Vallina, S. M., Ballabrera-Poy, J., Kettle, A. J., et al. (2011). An updated climatology of surface dimethylsulfide concentrations and emission fluxes in the global ocean. *Global Biogeochemical Cycles*, *25*, GB1004. <https://doi.org/10.1029/2010GB003850>
- Launois, T., Belviso, S., Bopp, L., Fichot, C. G., & Peylin, P. (2015). A new model for the global biogeochemical cycle of carbonyl sulfide—Part I: Assessment of direct marine emissions with an oceanic general circulation and biogeochemistry model. *Atmospheric Chemistry and Physics*, *15*(5), 2295–2312. <https://doi.org/10.5194/acp-15-2295-2015>
- Lennartz, S. T. (2017). From local to global scale—Marine emissions of the climate relevant sulfur gases carbonyl sulfide, carbon disulfide, and dimethyl sulfide, Ph.D. Thesis, Christian-Albrechts-Universität Kiel, Kiel, Germany
- Lennartz, S. T., Marandino, C. M., Hobe, M. V., Cortes, P., Quack, B., Simo, R., et al. (2017). Direct oceanic emissions unlikely to account for the missing source of atmospheric carbonyl sulfide. *Atmospheric Chemistry and Physics*, *17*(1), 385–402. <https://doi.org/10.5194/acp-17-385-2017>
- Marik, T. (1998). Atmospheric $\delta^{13}\text{C}$ and δD measurements to balance the global methane budget, PhD thesis, Ruprecht-Karls-Universität Heidelberg, Germany
- Maseyk, K., Berry, J. A., Billesbach, D., Campbell, J. E., Torn, M. S., Zahniser, M., & Seibt, U. (2014). Sources and sinks of carbonyl sulfide in an agricultural field in the Southern Great Plains. *PNAS*, *111*(25), 9064–9069. <https://doi.org/10.1073/pnas.1319132111>
- Mitchell, L. E., Buizert, C., Brook, E. J., Breton, D. J., Fegyveresi, J., Bagginstos, D., et al. (2015). Observing and modeling the influence of layering on bubble trapping in polar firn. *Journal of Geophysical Research: Atmospheres*, *120*, 2558–2574. <https://doi.org/10.1002/2014JD022766>
- Mitchell, L., Brook, E., Lee, J. E., Buizert, C., & Sowers, T. (2013). Constraints on the late Holocene anthropogenic contribution to the atmospheric methane budget. *Science*, *342*(6161), 964–966. <https://doi.org/10.1126/science.1238920>
- Montzka, S. A., Aydin, M., Battle, M., Butler, J. H., Saltzman, E. S., Hall, B. D., et al. (2004). A 350-year atmospheric history for carbonyl sulfide inferred from Antarctic firn air and air trapped in ice. *Journal of Geophysical Research*, *109*, D22302. <https://doi.org/10.1029/2004JD004686>
- Montzka, S. A., Calvert, P., Hall, B. D., Elkins, J. W., Conway, T. J., Tans, P. P., & Sweeney, C. (2007). On the global distribution, seasonality, and budget of atmospheric carbonyl sulfide (COS) and some similarities to CO_2 . *Journal of Geophysical Research*, *112*, D09302. <https://doi.org/10.1029/2006JD007665>
- Mühle, J., Trudinger, C. M., Western, L. M., Rigby, M., Vollmer, M. K., Park, S., et al. (2019). Perfluorocyclobutane (PFC-318, c-C4F8) in the global atmosphere. *Atmospheric Chemistry and Physics*, *19*(15), 10,335–10,359. <https://doi.org/10.5194/acp-19-10335-2019>
- Myhre, G., Berglen, T. F., Myhre, C. E. L., & Isaksen, I. S. A. (2004). The radiative effect of the anthropogenic influence on the stratospheric sulfate aerosol layer. *Tellus*, *56B*, 294–299
- Nicewonger, M. R., Verhulst, K. R., Aydin, M., & Saltzman, E. S. (2016). Preindustrial atmospheric ethane levels inferred from polar ice cores: A constraint on the geologic sources of atmospheric ethane and methane. *Geophysical Research Letters*, *43*, 214–221. <https://doi.org/10.1002/2015GL066854>
- Notholt, J., Kuang, Z., Rinsland, C. P., Toon, G. C., Rex, M., Jones, N., et al. (2003). Enhanced upper tropical tropospheric COS: Impact on the stratospheric aerosol layer. *Science*, *300*(5617), 307–310. <https://doi.org/10.1126/science.1080320>
- Patterson, J. D., Aydin, M., Crotwell, A. M., Petron, G., Severinghaus, J. P., & Saltzman, E. S. (2020). Atmospheric history of H_2 over the past century reconstructed from South Pole firn air. *Geophysical Research Letters*, *47*, e2020GL087787. <https://doi.org/10.1029/2020GL087787>
- Petrenko, V. V., Martinerie, P., Novelli, P., Etheridge, D. M., Levin, I., Wang, Z., et al. (2013). A 60 yr record of atmospheric carbon monoxide reconstructed from Greenland firn air. *Atmospheric Chemistry and Physics*, *13*(15), 7567–7585. <https://doi.org/10.5194/acp-13-7567-2013>
- Prentice, I. C., Harrison, S. P., & Bartlein, P. J. (2011). Global vegetation and terrestrial carbon cycle changes after the last ice age. *New Phytologist*, *189*(4), 988–998. <https://doi.org/10.1111/j.1469-8137.2010.03620.x>
- Protoschill-Krebs, G., & Kesselmeier, J. (1992). Enzymatic pathways for the metabolization of carbonyl sulphide (COS) by higher plants. *Botanica Acta: Journal of the German Botanical Society*, *105*, 206–212
- Protoschill-Krebs, G., Wilhelm, C., & Kesselmeier, J. (1996). Consumption of carbonyl sulfide (COS) by higher plant carbonic anhydrase (CA). *Atmospheric Environment*, *30*(18), 3151–3156. [https://doi.org/10.1016/1352-2310\(96\)00026-X](https://doi.org/10.1016/1352-2310(96)00026-X)
- Sandoval-Soto, L., Stanimirov, M., von Hobe, M., Schmitt, V., Valdes, J., Wild, A., & Kesselmeier, J. (2005). Global uptake of carbonyl sulfide (COS) by terrestrial vegetation: Estimates corrected by deposition velocities normalized to the uptake of carbon dioxide (CO_2). *Biogeosciences*, *2*(2), 125–132. <https://doi.org/10.5194/bg-2-125-2005>
- Severinghaus, J. P., Albert, M. R., Courville, Z. R., Fahnestock, M. A., Kawamura, K., Montzka, S. A., et al. (2010). Deep air convection in the firn at a zero-accumulation site, central Antarctica. *Earth and Planetary Science Letters*, *293*(3–4), 359–367. <https://doi.org/10.1016/j.epsl.2010.03.003>
- Sheng, J.-X., Weisenstein, D. K., Luo, B.-P., Rozanov, E., Stenke, A., Anet, J., et al. (2015). Global atmospheric sulfur budget under volcanically quiescent conditions: Aerosol chemistry-climate model predictions and validation. *Journal of Geophysical Research: Atmospheres*, *120*, 256–276. <https://doi.org/10.1002/2014JD021985>
- Smith, S. J., van Aardenne, J., Klimont, Z., Andres, R. J., Volke, A., & Arias, A. D. (2011). Anthropogenic sulfur dioxide emissions: 1850–2005. *Atmospheric Chemistry and Physics*, *11*(3), 1101–1116. <https://doi.org/10.5194/acp-11-1101-2011>
- Solomon, S., Daniel, J. S., Neely, R. R. III, Vernier, J. P., Dutton, E. G., & Thomason, L. W. (2011). The persistently variable “background” stratospheric aerosol layer and global climate change. *Science*, *333*(6044), 866–870. <https://doi.org/10.1126/science.1206027>
- Spivakovsky, C. M., Logan, J. A., Montzka, S. A., Balkanski, Y. J., Jones, D. B. A., Horowitz, L. W., et al. (2000). Three-dimensional climatological distribution of tropospheric OH: Update and evaluation. *Journal of Geophysical Research*, *105*(D7), 8931–8980. <https://doi.org/10.1029/1999JD901006>
- Stern, D. I. (2005). Global sulfur emissions from 1850 to 2000. *Chemosphere*, *58*(2), 163–175. <https://doi.org/10.1016/j.chemosphere.2004.08.022>
- Stimler, K., Berry, J. A., Montzka, S. A., & Yakir, D. (2011). Association between carbonyl sulfide uptake and $(18)\Delta$ during gas exchange in C(3) and C(4) leaves. *Plant Physiology*, *157*(1), 509–517. <https://doi.org/10.1104/pp.111.176578>
- Stimler, K., Montzka, S. A., Berry, J. A., Rudich, Y., & Yakir, D. (2010). Relationships between carbonyl sulfide (COS) and CO_2 during leaf gas exchange. *New Phytologist*, *186*, 869–878. <https://doi.org/10.1111/j.1469-8137.2010.03218.x>
- Sturges, W. T., Penkett, S. A., Barnola, J.-M., Chappellaz, J., Atlas, E., & Stroud, V. (2001). A long-term record of carbonyl sulfide (COS) in two hemispheres from firn air measurements. *Geophysical Research Letters*, *28*(21), 4095–4098. <https://doi.org/10.1029/2001GL013958>
- Suntharalingam, P., Kettle, A. J., Montzka, S. A., & Jacob, D. J. (2008). Global 3-D model analysis of the seasonal cycle of atmospheric carbonyl sulfide: Implications for terrestrial vegetation uptake. *Geophysical Research Letters*, *35*, L19801. <https://doi.org/10.1029/2008GL034332>

- Ulshöfer, V., & Andreae, M. O. (1998). Carbonyl sulfide (COS) in the surface ocean and the atmospheric COS budget. *Aquatic Geochemistry*, 3, 283–303
- van Aardenne, J. A., Dentener, F. J., Olivier, J. G. J., Klein Goldewijk, C. G. M., & Lelieveld, J. A. (2001). 1x1 resolution data set of historical anthropogenic trace gas emissions for the period 1890–1990. *Global Biogeochemical Cycles*, 15(4), 909–928. <https://doi.org/10.1029/2000GB001265>
- van der Werf, G. R., Randerson, J. T., Giglio, L., Collatz, G. J., Mu, M., Kasibhatla, P. S., et al. (2010). Global fire emissions and the contribution of deforestation, savanna, forest, agricultural, and peat fires (1997–2009). *Atmospheric Chemistry and Physics*, 10, 11,707–11,735
- Verhulst, K. R., Aydin, M., & Saltzman, E. S. (2013). Methyl chloride variability in the Taylor Dome ice core during the Holocene. *Journal of Geophysical Research: Atmospheres*, 118, 12, 218–12,228. <https://doi.org/10.1002/2013JD020197>
- Vernier, J.-P., Thomason, L. W., Pommerehne, J. P., Bourassa, A., Pelon, J., Garnier, A., et al. (2011). Major influence of tropical volcanic eruptions on the stratospheric aerosol layer during the last decade. *Geophysical Research Letters*, 38, L12807. <https://doi.org/10.1029/2011GL047563>
- Watts, S. F. (2000). The mass budgets of carbonyl sulfide, dimethyl sulfide, carbon disulfide and hydrogen sulfide. *Atmospheric Environment*, 34(5), 761–779. [https://doi.org/10.1016/S1352-2310\(99\)00342-8](https://doi.org/10.1016/S1352-2310(99)00342-8)
- Whelan, M. E., Lennartz, S. T., Gimeno, T. E., Wehr, R., Wohlfahrt, G., Wang, Y., et al. (2018). Reviews and synthesis: Carbonyl sulfide as a multi-scale tracer for carbon and water cycles. *Biogeosciences*, 15, 3625–3657. <https://doi.org/10.5194/bg-15-3625-2018>
- Wilke, C. R., & Lee, Y. (1955). Estimation of diffusion coefficients for gases and vapors. *Industrial & Engineering Chemistry*, 47(6), 1253–1257. <https://doi.org/10.1021/ie50546a056>
- Wohlfahrt, G. (2017). Commentary: Bi-directional COS exchange in bryophytes challenges its use as a tracer for gross primary productivity. *New Phytologist*, 215(3), 923–925. <https://doi.org/10.1111/nph.14658>
- Worton, D. R., Sturges, W. T., Reeves, C. E., Newland, M. J., Penkett, S. A., Atlas, E., et al. (2012). Evidence from firn air for recent decreases in non-methane hydrocarbons and a 20th century increase in nitrogen oxides in the northern hemisphere. *Atmospheric Environment*, 54, 592–602. <https://doi.org/10.1016/j.atmosenv.2012.02.084>
- Xu, X., Bingemer, H. G., & Schmidt, U. (2002). The flux of carbonyl sulfide and carbon disulfide between the atmosphere and a spruce forest. *Atmospheric Chemistry and Physics*, 2(3), 171–181. <https://doi.org/10.5194/acp-2-171-2002>
- Yvon, S. A., & Butler, J. H. (1996). An improved estimate of the ocean lifetime of atmospheric CH₃Br. *Geophysical Research Letters*, 23(1), 53–56. <https://doi.org/10.1029/95GL03022>
- Yvon, S. A., & Butler, J. H. (2002). Effect of oceanic uptake on atmospheric lifetimes of selected trace gases. *Journal of Geophysical Research*, 107(D20), 4414. <https://doi.org/10.1029/2001JD001267>
- Zumkehr, A., Hilton, T., Whelan, M., Smith, S., Kuai, L., Worden, J., & Campbell, J. E. (2018). Global gridded anthropogenic emissions inventory of carbonyl sulfide. *Atmospheric Environment*, 183, 11–19. <https://doi.org/10.1016/j.atmosenv.2018.03.063>